

Master's thesis

**A Study on Subtypes Clustering of
Glioma Image Using Cell Nuclei
Features**

Asami Yonekura

Division of Electrical and Electronic Engineering
Graduate School of Engineering
Mie University

Contents

1	Introduction	1
1.1	Background	1
1.2	Previous Studies and Problems	2
1.3	Objective	2
2	Experimental Materials	3
2.1	Glioma of the Brain Tumor	3
2.2	Obtained Histopathological Images	3
3	Experimental Methods	6
3.1	Construction of Image Data-set	6
3.2	Nuclei Segmentation	6
3.2.1	Pre-processing	8
3.2.2	Region Extraction	8
3.2.3	Nuclei Separation	11
3.3	Feature Descriptors	11
3.3.1	Object-Level Features	13
3.3.2	Spatial-Arrangement Features	13
3.4	Cluster Analysis	15
3.5	Statistical Test	18
4	Results and Discussion	21
4.1	Evaluation of Obtained Heat-map	21
4.2	Statistical Significance of Subtypes	21
5	Concluding Remarks	29
5.1	Conclusion	29
5.2	Further Works	29
	Acknowledgment	31

Reference	32
Publication List	36
Appendix A Results of Boxplot (GBM)	38
Appendix B Results of Boxplot (LGG)	45

List of Figures

2.1	Official website of The Cancer Genome Atlas (TCGA).	4
2.2	Samples of Glioma images obtained from TCGA database.	5
3.1	Criterion to collect patches for image data-set.	7
3.2	The pipeline for nuclei segmentation.	7
3.3	The examples of generated images by Pre-processing.	9
3.4	The examples of generated images by Region Extraction.	10
3.5	Basic overview of pixel values in the nuclei regions.	12
3.6	Nuclei segmented image.	12
3.7	Outline figures of Object-Level Features.	15
3.8	Outline figures of Spatial-Arrangement Features.	16
3.9	An example of heat-map.	19
3.10	An example of tree-structure of the hierarchy.	19
4.1	The obtained heat-map.	23
4.2	The estimated subtypes of GBM.	24
4.3	The estimated subtypes of LGG.	25
A.1	Boxplots of GBM (1)-(4).	38
A.2	Boxplots of GBM (5)-(10).	39
A.3	Boxplots of GBM (11)-(16).	40
A.4	Boxplots of GBM (17)-(22).	41
A.5	Boxplots of GBM (23)-(28).	42
A.6	Boxplots of GBM (29)-(34).	43
A.7	Boxplots of GBM (35)-(37).	44
B.1	Boxplots of LGG (1)-(4).	45
B.2	Boxplots of LGG (4)-(10).	46
B.3	Boxplots of LGG (11)-(16).	47
B.4	Boxplots of LGG (17)-(22).	48
B.5	Boxplots of LGG (23)-(28).	49
B.6	Boxplots of LGG (29)-(34).	50
B.7	Boxplots of LGG (35)-(37).	51

List of Tables

3.1	List of Object-Level Features.	14
3.2	List of Spatial-Arrangement Features.	17
4.1	The utilized features list.	22
4.2	Statistical significance of GBM	27
4.3	Statistical significance of LGG	28

Chapter 1

Introduction

1.1 Background

Evaluations of surgical biopsy, postmortem tissue specimens for the diagnosis and understanding of human disease are one of the critical components for biomedical studies. Currently, these analyses are manually performed by specialists. In some cases, the evaluation of the pathology images, however, requires many specialists (=pathologists) to decide the category of the specific disease, or its subtype or grade. Central problems in this process have

- the number and variability of disease tissue specimens,
- the inability to perform cross comparison analyses, and
- frequent lack of agreement between different pathologists.

In addition, precise and practical integration of definitive histopathological image-based data with that of genetic, genomic, clinical data is critical for precision medicine. Doing this will need rigorous and reproducible multidimensional characterizations of surgical pathology samples. Therefore, the need for quantitative analysis methods for classifications of disease types, subtypes and grading the stage of the disease progression has been growing. For these goals, many recent developments in biomedical informatics use computer vision techniques for computational pathology [1–5].

Moreover recently, the researches addressing both genomics and phenomics have been proposed [6–9]. K. T. Zondervan produced consensus data and sample collection protocols for endometriosis research and integrating phenomic with genomic data to identify informative subtypes of endometriosis [6]. These research reports show progress to enhance understanding of the pathogenic mechanisms of the disease and discovery of novel, targeted treatments.

1.2 Previous Studies and Problems

Our research group is currently addressing the problem of recognizing and extracting quantitative features from Glioma histopathological images by defining, counting, and measuring morphological characteristics that can serve as fundamental data elements capable of distinguishing key disease types and subtypes. In the past papers, we focused on Glioma, which was one of the brain tumors, and proposed nuclei segmentation, feature extraction, and disease stage classification methods for Glioma images [10, 11]. We also discussed which feature descriptors are significant for disease stage classification in Glioma images [12]. However, we evaluated only two distinct type of classification performance, *i.e.* Glioblastoma (GBM) or Low Grade Glioma (LGG). In fact, subtypes of Glioma is not specified so far. However, disease stages of Glioma are determined by a combination of genes. Therefore, even if the given tissue images belong to the same grade, the patterns of gene expression are different among patients. Thus, the next step of this study is to (i) analyze the relationships between patterns of genes expression and the feature descriptors and (ii) to find out new subtypes of Glioma by using the obtained knowledge. The final goal of our research, I specify subtypes of Glioma from histopathological images for precision medicine by genes expressions level.

1.3 Objective

In this thesis, phenomics analyses were focused as the first step for the final goal of our research. In particular, feature descriptors related to the region of nuclei that were regarded as effective for evaluation of Glioma in the previous studies were utilized. This work discusses about

- method of nuclei segmentation using custom-designed image processing,
- the heat-maps to estimate which Glioma images have been grouped based on their pattern of the feature descriptors as subtypes, and
- a statistical test to confirm whether these feature descriptors had the capability to distinguish the sub-types that were estimated.

Chapter 2

Experimental Materials

2.1 Glioma of the Brain Tumor

This study deals with the histopathological images of Glioma, which is one of the malignant tumors of the brain. Glioma begins in the gluey supportive cells (glial cells) that support nerve cells. Generally, Glioma can be categorized into four grades based on their disease stage. For example, Grade 1 has a slight illness, and Grade 4 is so serious and has a poor prognosis. In particular, the average life expectancy of Grade 4 is approximately 18 months. Furthermore, it is quite difficult to remove all of them by surgery because of infiltration growth. For that reason, effective treatment by each stage of Glioma progression is required.

2.2 Obtained Histopathological Images

This study used Glioma images obtained from The Cancer Genome Atlas (TCGA) [13] database as experimental materials (Figure 2.1). TCGA is co-managed by the National Cancer Institute (NCI) and the National Human Genome Research Institute (NHGRI) scientists and managers. TCGA researchers have analyzed over 30 human tumors and provide publicly available data-sets to help improve diagnostic methods, treatment standards, and finally to prevent cancer [14].

Glioma images archived in TCGA database were categorized into 2 types, *i.e.* Lower-Grade-Glioma (LGG) and Glioblastoma multiforme (GBM). LGG includes images of Grades 1 and 2, GBM includes images of Grades 3 and 4. Figure 2.2 shows samples of LGG and GBM images obtained from TCGA database. These images were stained by Hematoxylin and Eosin (H&E) staining method. Generally, Hematoxylin makes nuclei deep purple and Eosin does other tissues pale purple and red.

As seen in Figure 2.2, the grade of the disease progression seems to correlate with some image features, such as nuclei properties of size, shapes, density, and typology. In addition, these correlations are believed to result from the disease progression, including

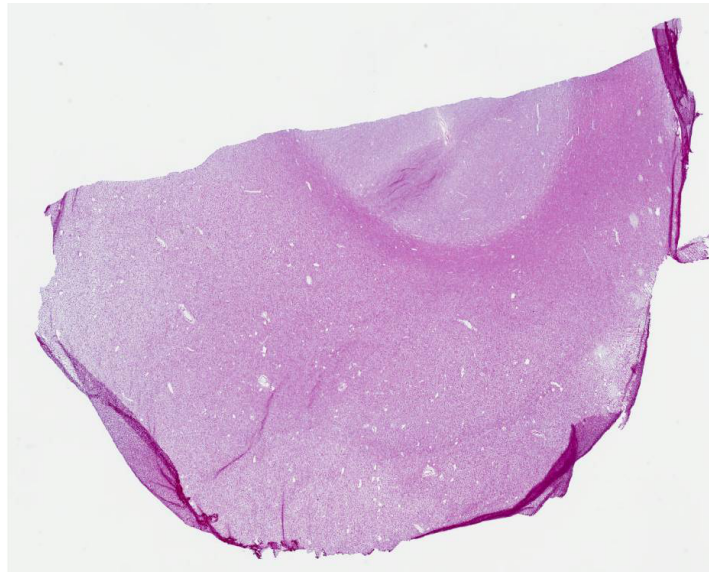
The screenshot shows the official website of The Cancer Genome Atlas (TCGA). At the top, the NIH logo is on the left, and the text "THE CANCER GENOME ATLAS National Cancer Institute National Human Genome Research Institute" is in the center. To the right, there are links for "Launch Data Portal", "Contact Us", and "For the Media", along with a search bar. Below the header is a navigation menu with links: "Home", "About Cancer Genomics", "Cancers Selected for Study", "Research Highlights", "Publications", "News and Events", and "About TCGA".

The main content area features a section titled "TCGA's Study of Soft Tissue Sarcoma". It includes a diagram showing the integration of data from various platforms (LMS, BOLFS, LFS, MPMET) and the resulting genomic insights. The text states: "TCGA's analysis of six major types of adult soft tissue sarcomas reveals frequent copy number alterations, low mutational loads, and a diverse array of underlying molecular mechanisms. Certain sarcomas may benefit from immunotherapy." Below this, there are several sub-sections: "Liposarcomas", "Soft tissue sarcoma", "Myofibroblastic Undifferentiated Pleomorphic Sarcoma", and "Dedifferentiated Liposarcoma".

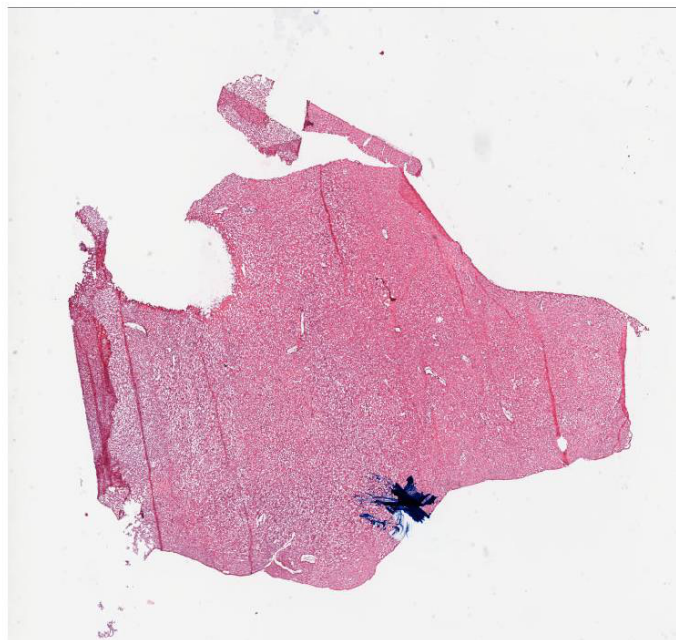
On the right side, there is a "Launch Data Portal" button and a section titled "Questions About Cancer" with links to "Visit www.cancer.gov", "Call 1-800-4-CANCER", and "Use LiveHelp Online Chat". Below that is a "Multimedia Library" section with links to "Images" and "Videos and Animations".

Figure 2.1: Official website of The Cancer Genome Atlas (TCGA).

changes in gene and protein expression. Therefore, these features in the images were used for analysis in the study of biomedical informatics.



(a) Lower-Grade-Glioma (LGG) (Size: 30001×23980 pixels)



(b) Glioblastoma multiforme (GBM) (Size: 33958×36141 pixels)

Figure 2.2: Samples of Glioma images obtained from TCGA database.

Chapter 3

Experimental Methods

3.1 Construction of Image Data-set

In this study, two type data-sets, *i.e.* LGG and GBM, were constructed for experiments. At first step, 100 Glioma histopathological images in each category were downloaded from TCGA database. These images will be not good for processing because these sizes are large (approximately 30000×30000 pixels). Therefore, these images were divided into patches whose sizes were 2000×2000 pixels. Subsequently, patches including the sufficient number of nuclei were collected as shown in the Figure 3.1. In this study, 30 collected patches in each original images (total 6000 patches) were used as data-sets.

3.2 Nuclei Segmentation

After data-set construction, a nuclei segmentation method was applied to the given images to extracted features from them. For nuclei segmentation, this study employed CellProfiler [15, 16], which is an open source software developed by Broad Institute. This software is a tool for exploring and visualizing multidimensional data that has been extracted from biological images automatically. This software enables to measure the size, shape, intensity, and texture of object (*e.g.* cells, colonies, and so on) in every image. Figure 3.2 shows the pipeline of nuclei segmentation method and it mainly consists of three steps as follows:

1. Pre-processing
2. Region Extraction
3. Nuclei Separation

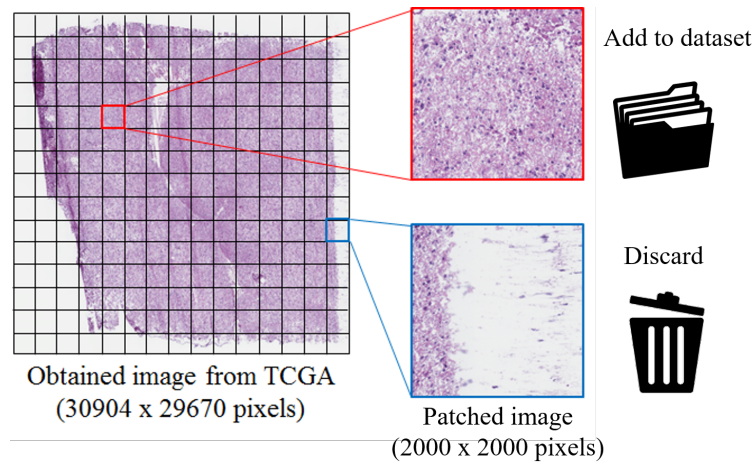


Figure 3.1: Criterion to collect patches for image data-set.

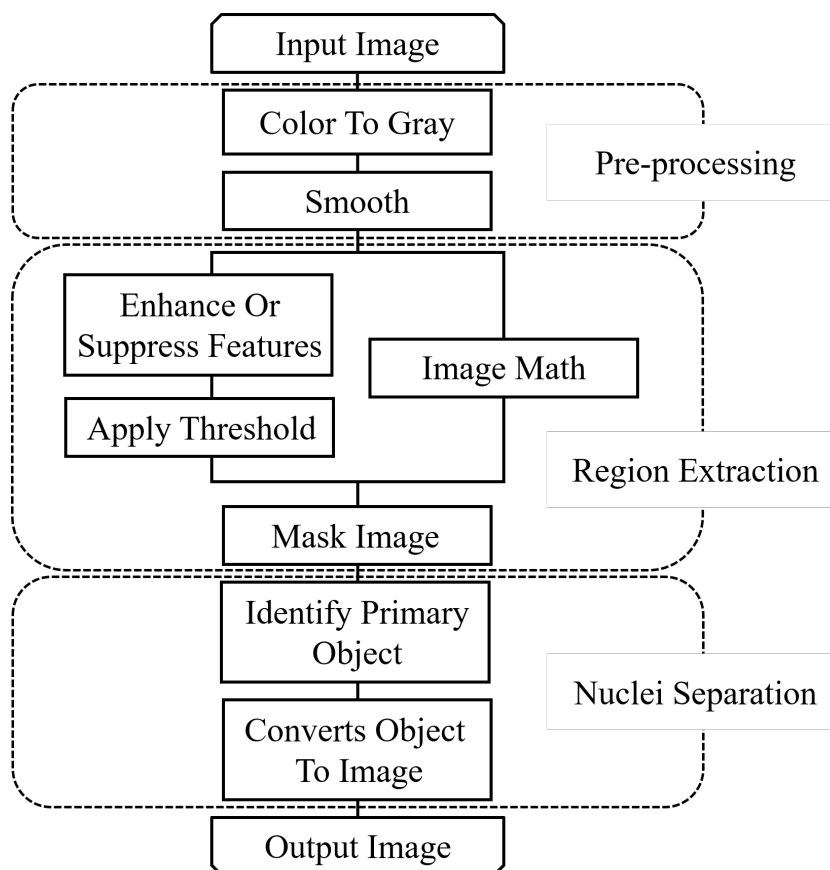


Figure 3.2: The pipeline for nuclei segmentation.

3.2.1 Pre-processing

The first step consists of two modules, *Color To Gray* and *Smooth*. Figure 3.3 shows the examples of images corresponding to each step. *Color To Gray* module converts the image with multiple color channels to gray-scale. When the color image is converted to gray-scale in this module, we can adjust the contribution of the colors relative to each other. In this thesis, this module was set to contribute the red channels for H&E staining images (Figure 3.3 (b)).

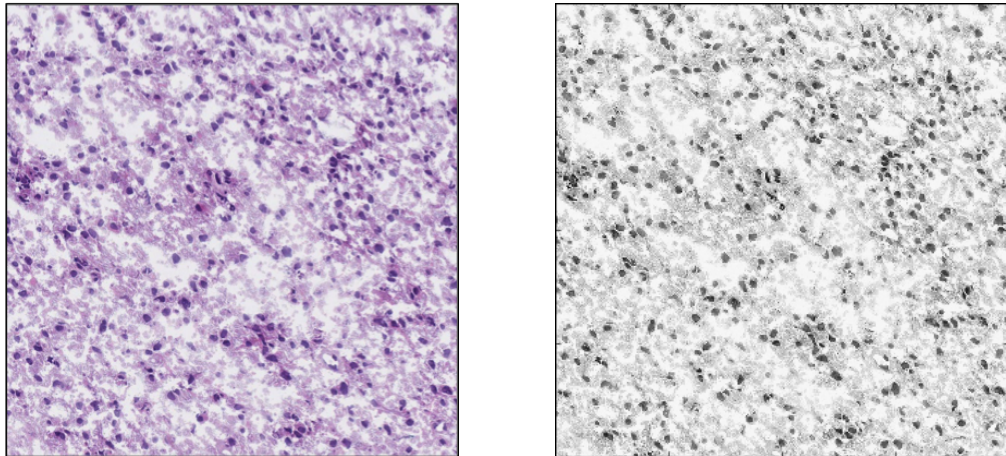
Smooth module smooths away the image to remove small artifacts, *e.g.* a bubble on the cell nuclei in the image. In this module, Smooth Keeping Edges is applied as a smoothing method to retain edges in the image while smoothing other features. This image processing technique utilizes a bilateral filter that limits Gaussian smoothing across an edge while applying smoothing perpendicular to an edge (Figure 3.3 (c)). Fuzzy smoothing and adaptive thresholding techniques [17,18] were referenced to improve these preliminary this step.

3.2.2 Region Extraction

After the above step, nuclei in the image were roughly segmented. This step consists of four modules, *Enhance Or Suppress Features*, *Apply Threshold*, *Image Math*, and *Mask Image*. In addition, the image was processed to two sub-pipelines independently in order to produce a rough segmentation image. Figure 3.4 shows the examples of images in each process.

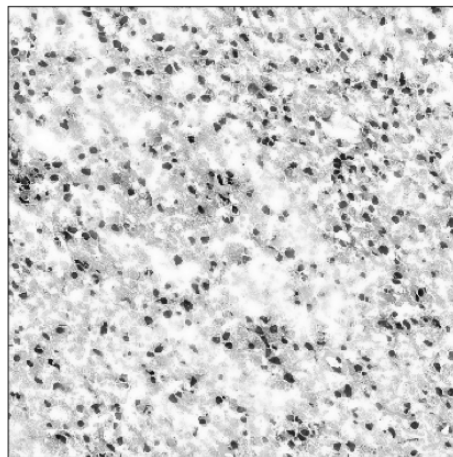
Enhance Or Suppress Features module enhances or suppresses certain image features (such as speckles, ring shapes, and neurites) by applying filters to the image. It produces a gray-scale image in which objects can be identified using *Identify* module. In this study, *Enhance* operation was selected to emphasize dark areas because the region of nuclei was dark compared with other tissue areas. This operation utilizes morphological reconstruction (the rolling-ball algorithm) to identify dark holes within brighter areas or ring shapes. As a result, the image is inverted so that the dark holes turn into bright peaks (Figure 3.4 (a)).

Apply Threshold module produces a binary image based on a threshold that can be selected beforehand or calculated automatically. The threshold value is determined based on the pixel intensities by threshold strategy and then, CellProfiler can select this strategy, *e.g.* Global, Adaptive, Per Object, and so on. In this study, Adaptive was applied and it partitions the image into tiles and calculate thresholds for each tile. In addition, CellProfiler can select the threshold methods for binarizing, *e.g.* Otsu, MoG, Kapur, and so on. Otsu was applied in this case and it calculates the threshold to separate pixels (foreground and background) with discriminant analysis. After the threshold value



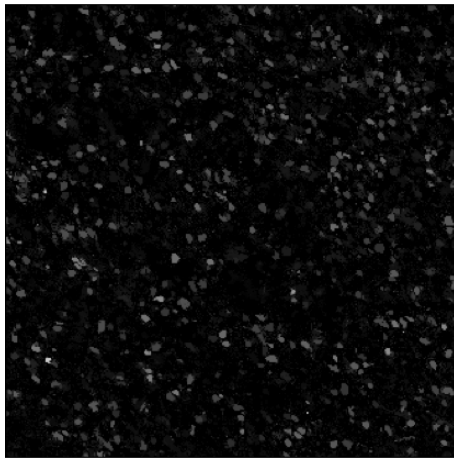
(a) Input Image

(b) Gray-scaled Image

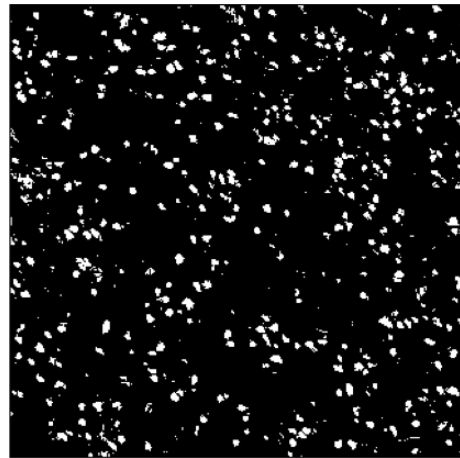


(c) Smoothed Image

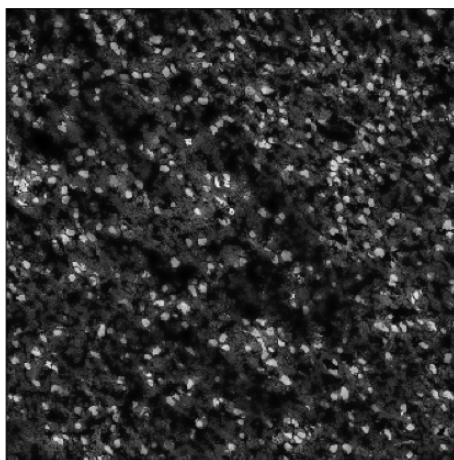
Figure 3.3: The examples of generated images by Pre-processing.



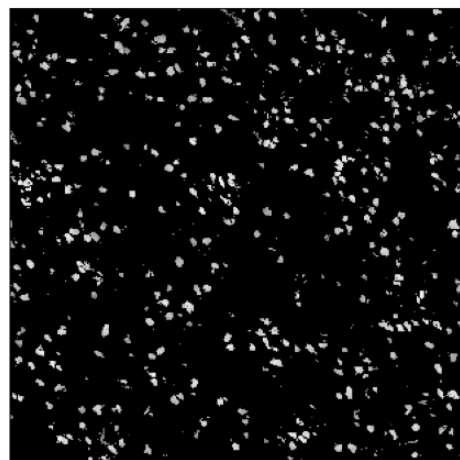
(a) Enhanced & Inverted Image



(b) Binarized Image



(c) Only Inverted Image



(d) Superimposed Image

Figure 3.4: The examples of generated images by Region Extraction.

has been determined, the image is set pixel intensities below the value to zero (black) and above the value to one (white) by this module (Figure 3.4 (b)). These modules were used in the first sub-pipeline to extract nuclei regions roughly from the image, but adjacent nuclei are grouped as one nucleus.

In the second sub-pipeline, the inverted image is produced by using *Image Math* module to separate the adjacent nuclei regions. This module can perform addition, subtraction, multiplication, division, or averaging of two or more image intensities, as well as inversion, log transform, or scaling by a constant for individual image intensities. In this study, inversion was selected as the operation of this module and image intensities was inverted(Figure 3.4 (c)).

After independent sub-pipelines processing, the rough segmented image was produced by superimposing the binary image (Figure 3.4 (b)) and the inverted image (Figure 3.4 (c)) and then, *Mask Image* module is applied to superimpose them. Figure 3.4 (d) is an example of superimposed image given by *Mask Image* module.

3.2.3 Nuclei Separation

The final step consists of two modules, *Identify Primary Objects* and *Converts Object To Image*. The obtained image still had adjacent nuclei regions, therefore, nuclei should be separated for accurate feature extraction. Therefore, *Identify Primary Objects* module was applied to determine the boundary of them. This module identifies biological components of interest in gray-scale images containing bright objects on a dark background. When the objects have some peaks of brightness, this module counts each peak point as an individual object and the object centers are defined as local intensity maximum in the image. In Figure 3.5, an adjacent nucleus region has plural peaks, thus, adjacent nuclei regions are separated into each nucleus based on the distribution of pixel values by applying this module.

Finally, *Converts Object To Image* module colored each separated nucleus for recognition. Figure 3.6 shows the result of nuclei segmented image. The effectiveness of this procedure was confirmed for this task in literature [19].

3.3 Feature Descriptors

Feature descriptors for analyzing histopathological images are mainly categorized into two types [20] as follows;

1. Object-Level Features, and
2. Spatial-Arrangement Features.

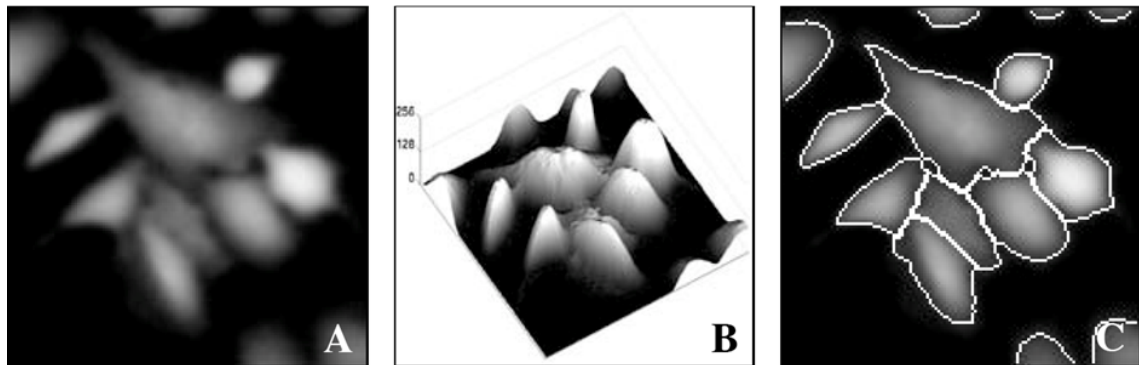


Figure 3.5: Basic overview of pixel values in the nuclei regions.

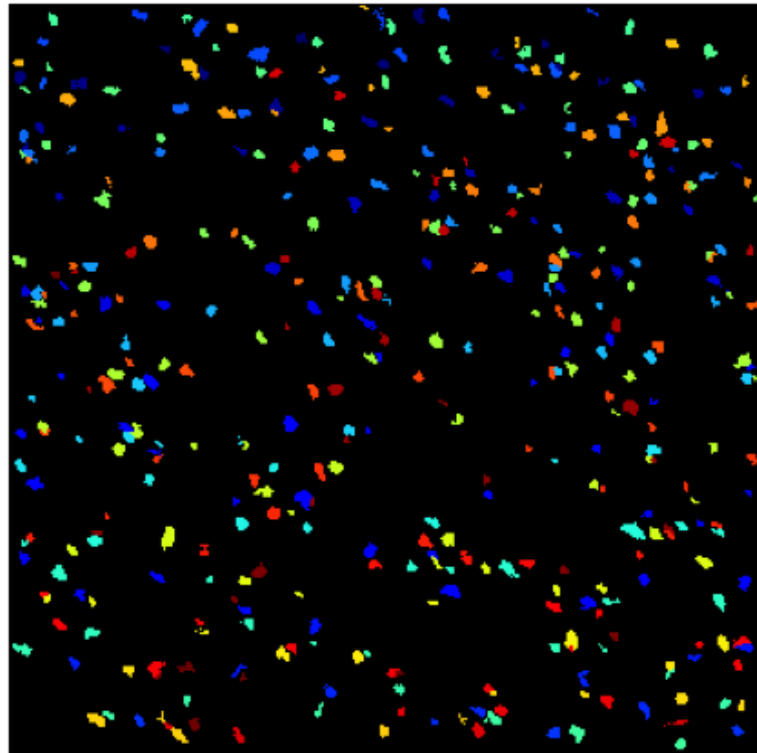


Figure 3.6: Nuclei segmented image.

These features has been discussed and confirmed their effectiveness for evaluation of subtypes of Glioma in literature [21,22].

3.3.1 Object-Level Features

Object-Level Features are directly related to the size and shape of each object, such as a nucleus. These features were classified to the following types.

- **Original Features** are the total amount of pixels in the segmented nucleus. Number of nuclei and Area of a nucleus are utilized as the feature descriptors.
- **Elliptical Features** are generated from an approximated ellipse of each nucleus. Subsequently, the Major and Minor Axis Length, Eccentricity, Orientation, Elliptical Deviation, Extent and Aspect Ratio are calculated.
- **Convex Hull Features** are generated from convex hull of the mask of each nucleus and calculate Convex Area, Convex Deficiency and Solidity.
- **Bounding Box Features** are calculated with the bounding box, which is defined as the smallest rectangle that completely contains the object mask, where the sides of the rectangle are aligned with the image axes. Extent and Aspect Ratio are utilized as the feature descriptors.
- **Boundary Features** are related to the boundary of the object. Thus in this study, these features are related to the perimeter of the nucleus.

The examples of outline figures are shown in Figure 3.7 and Table 3.1 shows all of the extracted Object-Level Features.

3.3.2 Spatial-Arrangement Features

Spatial-Arrangement Features are feature descriptors with respect to the topographical positions of nuclei. To get these features, a nucleus is called a node and graphs that connect the nodes are constructed [23–25]. For instance, B. Weyn used fractal and syntactic structure analysis (SSA), and he took into account the spatial-arrangement features [23]. Furthermore, he applied SSA to malignant mesothelioma images [24]. Another report shows a method to make perceptual boundaries of relatively homogeneous dot patterns. Generally, Spatial-Arrangement Features do not depend on the shapes of segmented nuclei, but their positions and distances among nodes. Such topological features can be also valiant descriptors to express the Spatial-Arrangement of nodes.

In this study, the following types graph are utilized for analyses [26]. Feature descriptors obtained from these graphs are extracted. Samples of an input image and the

Table 3.1: List of Object-Level Features.

Types	Features
Original	Number of nuclei, Area
Elliptical	Major Axis Length Minor Axis Length Eccentricity Orientation Elliptical Deviation Extent Aspect Ratio
Convex Hull	Convex Area Convex Deficiency Solidity
Bounding Box	Extent Aspect Ratio
Boundary	Perimeter Radii Perimeter Curvature
Other Shape	Equivalent Diameter Sphericity Compactness Inertia Shape

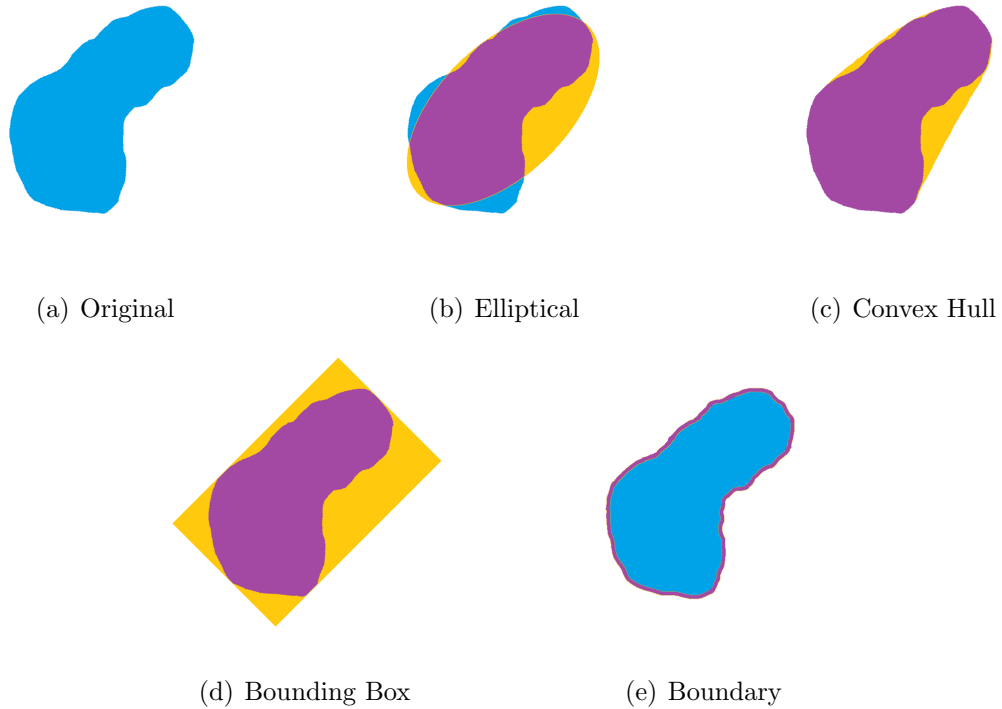


Figure 3.7: Outline figures of Object-Level Features.

constructed graphs are shown in Figure 3.8. Incidentally, the circle marks indicate the nodes located at gravity centers of each of the nuclei.

- **Voronoi Tessellation (VT)** is obtained from the input image and the perpendicular bisectors of nodes are connected to each other. As shown in Figure 3.8 (b), the obtained graph has many regions that are surrounded by perpendicular bisectors.
- **Delaunay Triangulation (DT)** is constructed by connecting the nodes of the neighboring boundary region in Voronoi Tessellation. Therefore, these graphs are expected to show the adjacency relationship of the Voronoi regions.
- **Minimum Spanning Tree (MST)** is obtained by connecting all of the nodes in the graphs with the minimum edge length of Delaunay Triangulation.

All of the extracted Spatial-Arrangement Features are shown in Table 3.2 [26].

3.4 Cluster Analysis

In this study, the heat-map was used to estimate which images have been grouped based on their patterns of the feature descriptors. Heat-map is often used for visualizing

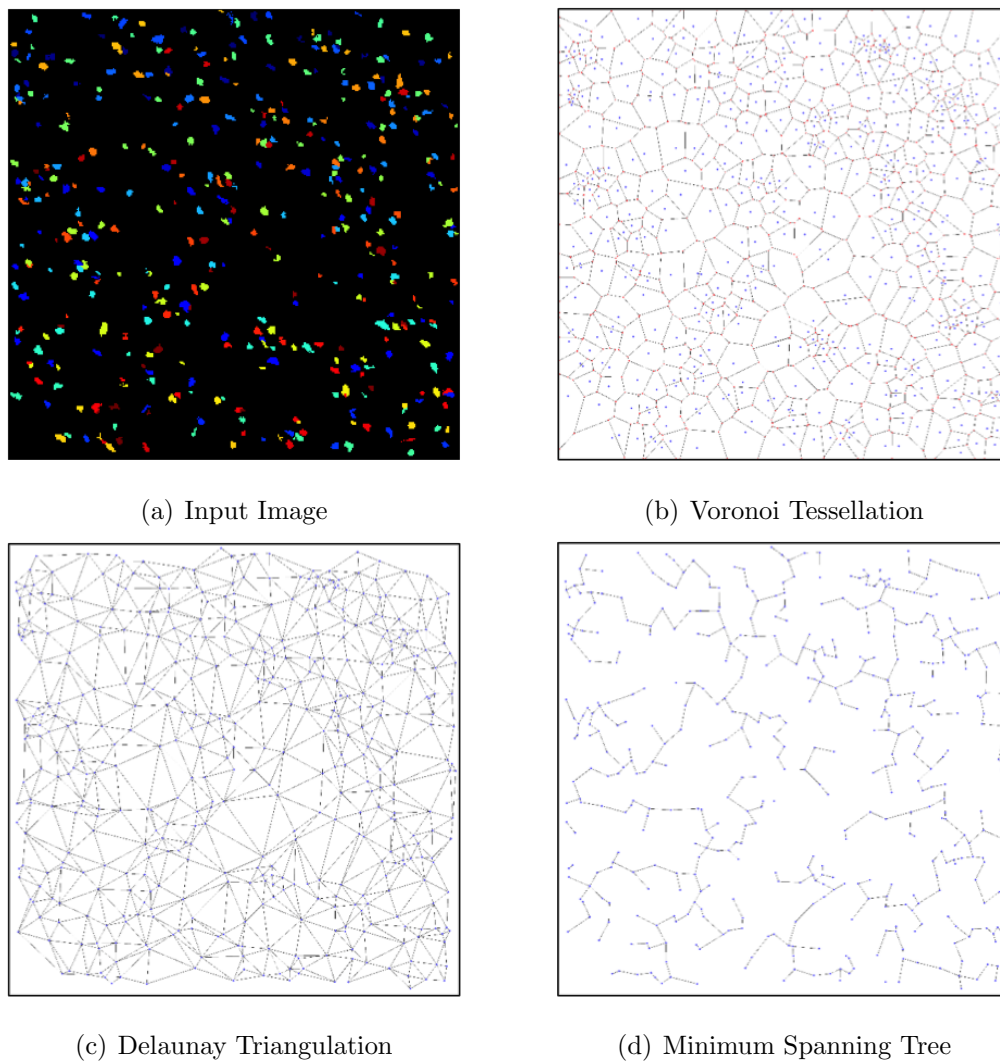


Figure 3.8: Outline figures of Spatial-Arrangement Features.

Table 3.2: List of Spatial-Arrangement Features.

Types	Features
Voronoi Tessellation	Number of Nodes Number of Edges Edge Length Cyclomatic Number Number of k-Walks Degree Spectral Radius Randic Index Area Area Disorder Perimeter Roundness Factor Homogeneity
Delaunay Triangulation	Number of Nodes Number of Edges Edge Length Cyclomatic Number Number of Triangles Number of k-Walks Degree Spectral Radius Randic Index
Minimum Spanning Tree	Number of Nodes Number of Edges Edge Length Degree Spectral Radius Randic Index

and interpreting based on the similarity of their gene expression pattern, as well as phenomics data in the biomedical informatics [27–32]. This method is useful for identifying genes or biological signatures associated with a particular condition.

Generally, a heat-map express the given data as a two-dimensional map shown as Figure 3.9. In the map, the vertical axis means feature descriptors and the horizontal axis is the given images. For instance, the top-left cell shows the normalized value of Feature A about Image A. The color of the cell corresponds to the feature value - red and blue mean high and low values, respectively.

In this study, Morpheus [33] was employed to visualize the feature descriptors extracted from the images. This software can visualize the given data-set as a heat-map and have various functions, *e.g.* the cluster, create new annotations, search, filter, sort, display charts, and more. In the cluster, it supports hierarchical and k-means clustering. In addition, there are multiple choices of the dissimilarity metrics, *e.g.* Euclidean, Jaccard, and so on. In this study, hierarchical clustering with Euclidean distance was selected. This is defined by

$$d_{ij} = \sqrt{\sum_{k=1}^K (x_{ik} - x_{jk})^2} \quad (3.1)$$

where \vec{x}_i is the i^{th} K-dimension feature vector defined as $[x_{i1}, x_{i2}, \dots, x_{iK}]$. And then, median feature values were picked up from each 30 collected patches because of dispersion fall in each TCGA data. The result of the clustering shows the similarity between the given data-set depending on these feature values.

And then, a tree-structure of the hierarchy are created as shown in Figure 3.10. Therefore, the images can be grouped and estimate subtypes by analyzing the heat-map.

3.5 Statistical Test

To confirm whether these feature descriptors can distinguish the estimated subtypes, this chapter discussed statistical significance of these features. In this study, Tukey’s range test was employed to evaluate their statistical significance.

Tukey’s range test is a single-step multiple comparison procedure and statistical test [34]. This method compares the means of every cohort to the means of every other cohort. This is defined by

$$q_T = \frac{\bar{x}_1 - \bar{x}_2}{s\sqrt{\frac{1}{n}}} \quad (3.2)$$

where \bar{x}_1 and \bar{x}_2 are the two mean values for comparison, n is the sample size, and s is

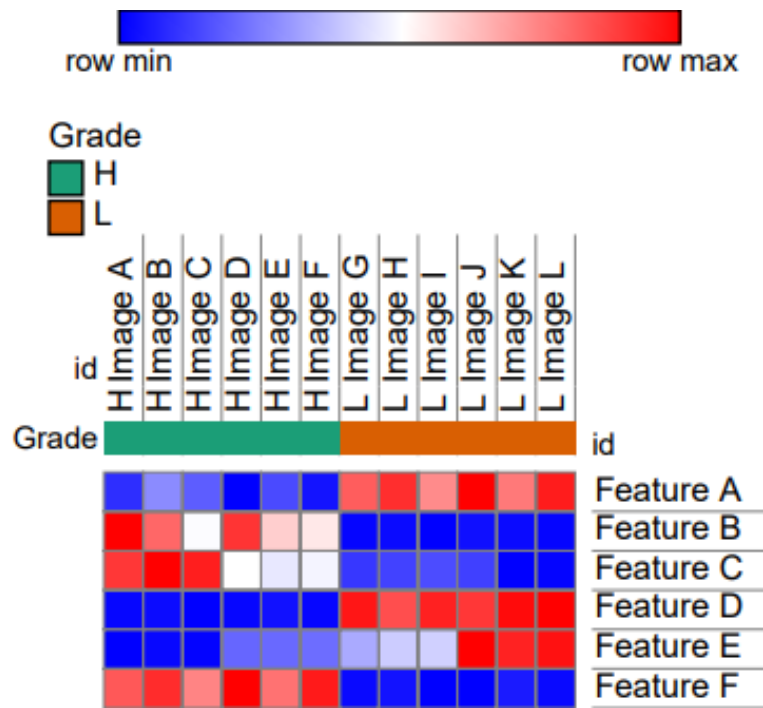


Figure 3.9: An example of heat-map.

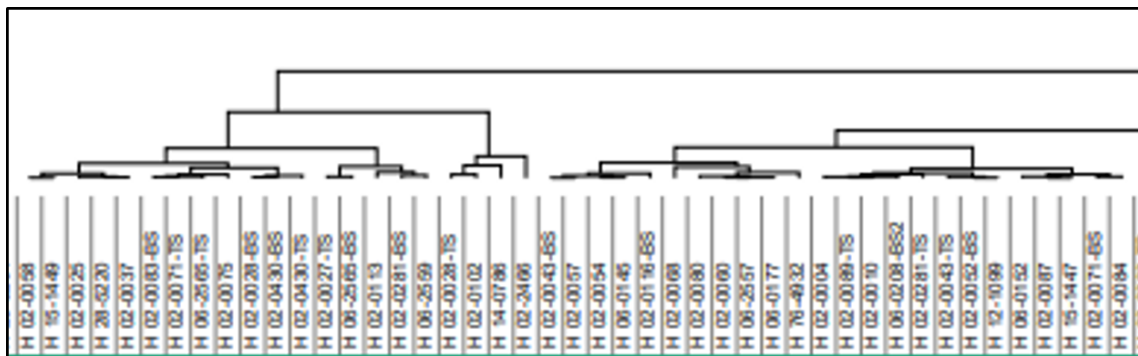


Figure 3.10: An example of tree-structure of the hierarchy.

standard deviation. This is defined by

$$s = \sqrt{\frac{1}{n} \sum_{i=1}^n (x_i - \bar{x})^2} \quad (3.3)$$

where x_i is each sample value and \bar{x} is the mean value. Then, this q_T value is compared to a q value from the studentized range distribution. If the q_T value is larger than the critical q value obtained from the distribution, the two means are significantly different.

However, the sample sizes must be equal when using the studentized range approach. Nevertheless, the sample sizes i.e. estimated subtypes sizes, are unequal in the case of this study. In this case, the estimated standard deviation should be calculated for each pairwise comparison, and it referred to as the Tukey–Kramer test formalized by Clyde Kramer [35]. Therefore, Tukey-Kramer test was employed in this study. This is defined by

$$q_{TK} = \frac{\bar{x}_1 - \bar{x}_2}{s \sqrt{\frac{1}{n_1} + \frac{1}{n_2}}} \quad (3.4)$$

where n_1 and n_2 mean the sizes of group 1 and 2, respectively. q_{TK} value is also compared to a q value from the studentized range distribution.

In this study, these algorithms were implemented by “R 3.5.1”, which was a software for statistical analysis. The significance level was set to 0.01. If the obtained p value was satisfied with the above criterion, thus it was regarded that the feature descriptor had sufficient capability to distinguish the estimated subtypes.

Chapter 4

Results and Discussion

4.1 Evaluation of Obtained Heat-map

In this thesis, 37 feature descriptors that selected from the previous research were utilized [12]. In the previous research, 58 features were utilized for disease stage classification of Glioma. These were judged as effective features for evaluation of subtypes of Glioma in literature [21, 22]. Table 4.1 shows the list of utilized features.

Figure 4.1 shows the obtained heat-map. As you can see, this heat-map varied clearly in color and it could be roughly divided into some groups. The result of a hierarchical clustering is displayed as a heat-map as a dendrogram, which is a tree-structure of the hierarchy. Some groups could categorize by analyzing these dendrograms. These dendrograms were analyzed following the advice by specialists who are research collaborators. Thus, subtypes of Glioma were estimated to 18 groups, *i.e.* 10 GBM and 8 LGG subtypes, depending on this dendrogram as shown in Figures 4.2 and 4.3. These subtypes are estimated at the bottom of the heat-maps.

4.2 Statistical Significance of Subtypes

Tables 4.2 and 4.3 show the results of statistical tests about GBM and LGG. Furthermore, the result of boxplots were shown in Appendix A (GBM) and B (LGG). As a result of experiments, 24 features were significant statistically to distinguish estimated LGG subtypes. On the other hand, there were no significant feature descriptor in the case of GBM. Furthermore, 7 features were statistically significant between D1 and D2 but most features were not. However, each subtype of GBM could be specified by combing several features. When some features were taken together, all of the estimated subtypes were divided into significantly each group.

Actually, in the previous research [12], Object-Level Features and Spatial-Arrangement Features were used for classification of Glioma. The result of the previous research indicates that Object-Level Features worked well compared to Spatial-Arrangement Fea-

Table 4.1: The utilized features list.

Types	Features
Original	Area
Boundary	Radii Perimeter Curvature
Convex Hull	Convex Deficiency
Elliptical	Minor Axis Length Eccentricity Orientation
Other Shapes	Sphericity
Voronoi Tessellation	Number of Nodes Number of Edges Randic Index Cyclomatic Number Number of k-Walks Degree Area Perimeter Roundness Factor
Delaunay Triangulation	Number of Nodes Number of Edges Edge Length Cyclomatic Number Number of Triangles Number of k-Walks Degree Spectral Radius Randic Index
Minimum Spanning Tree	Number of Nodes Edge Length Randic Index Degree

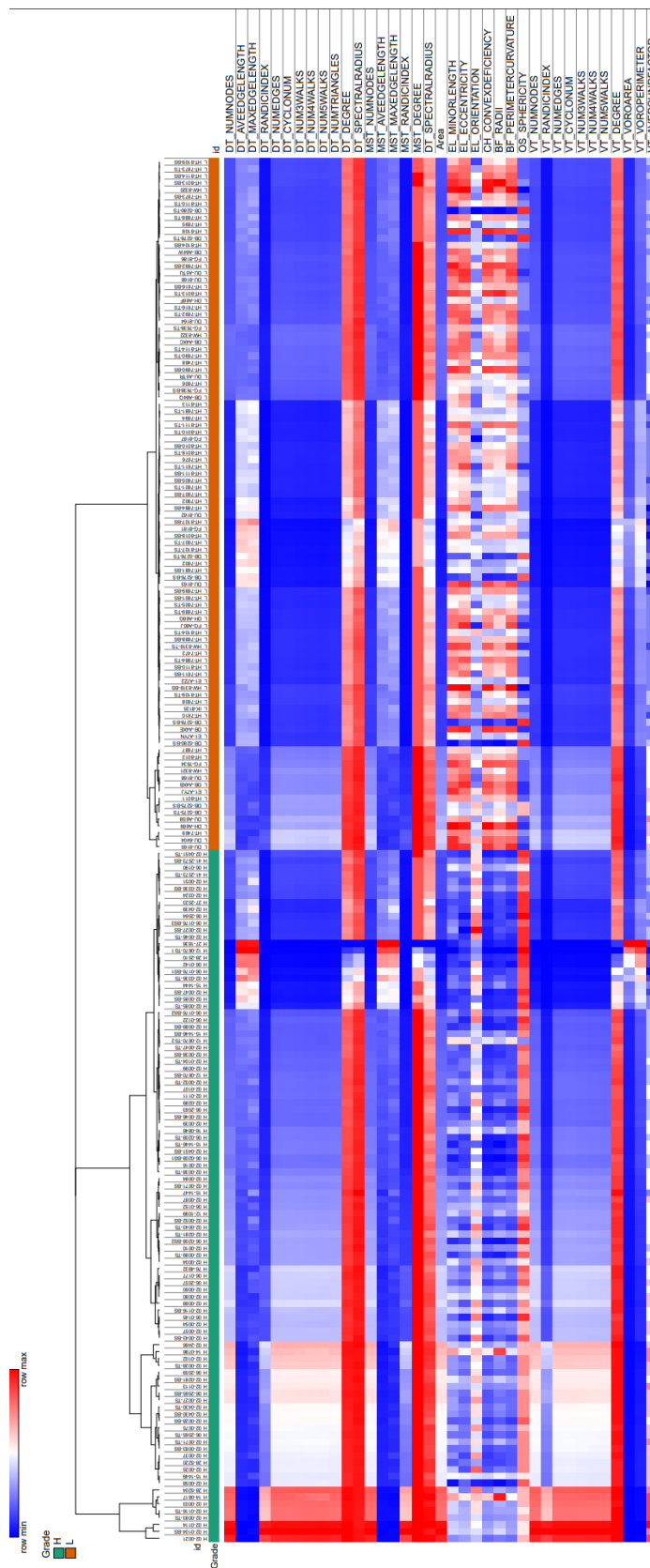


Figure 4.1: The obtained heat-map.

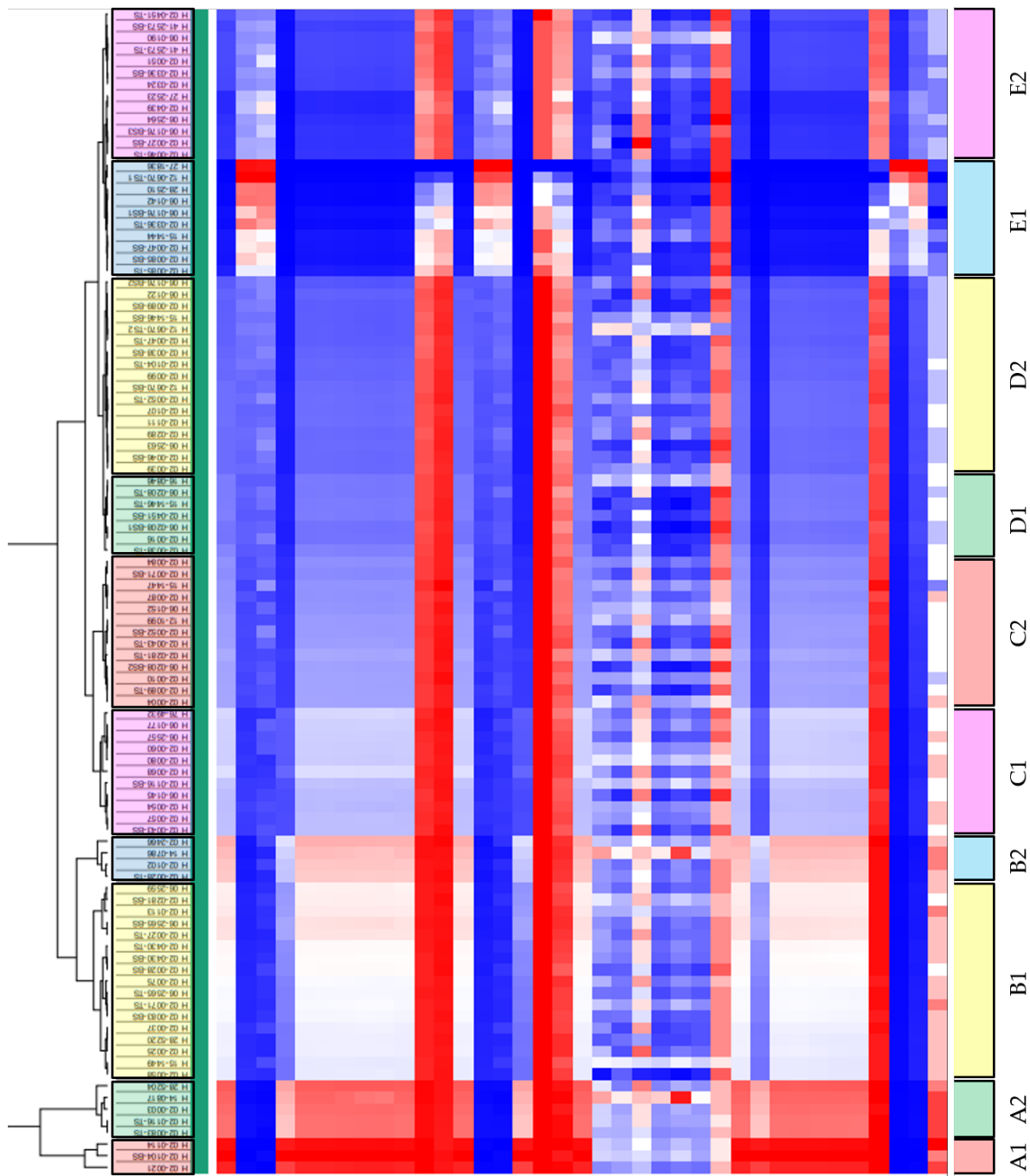


Figure 4.2: The estimated subtypes of GBM.

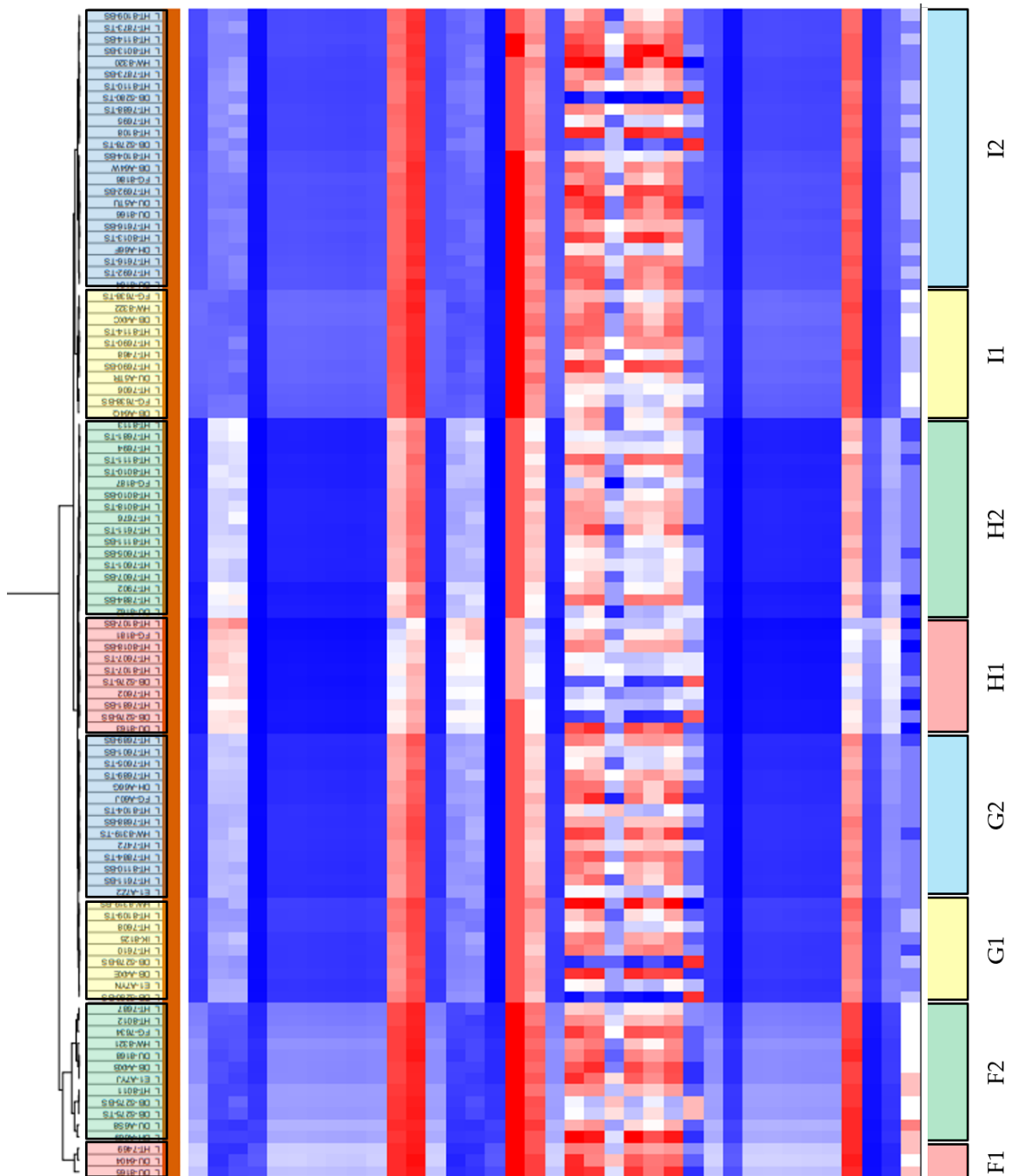


Figure 4.3: The estimated subtypes of LGG.

tures for disease stage classification. However, the result of this thesis indicates that most Spatial-Arrangement Features have meaningful information for subtypes clustering but most Object-Level Features were not significant. It suggested that the feature types have to change depending on the situations of classification, and Spatial-Arrangement Features are important to proceed advance researches, *e.g.* subtypes clustering.

Table 4.3: Statistical significance of LGG

		Features																																													
		Area	BF-PERIMETERCURVATURE	BF-RADII	CH-CONVEXDEFICIENCY	DT-AVEEDGELENGTH	DT-CYCLONUM	DT-DEGREE	DT-MAXEDGELENGTH	DT-NUM3WALKS	DT-NUM4WALKS	DT-NUM5WALKS	DT-NUM6WALKS	DT-NUMNODES	DT-NUMTRIANGLES	DT-RANDICINDEX	DT-SPECTRALRADIUS1	DT-SPECTRALRADIUS2	EL-ECCENTRICITY	EL-MINORLENGTH	EL-ORIENTATION	MST-AVEEDGELENGTH	MST-DEGREE	MST-MAXEDGELENGTH	MST-NUMNODES	MST-RANDICINDEX	OS-SPHERICITY	VT-AVEROUNDFACTOR	VT-CYCLONUM	VT-DEGREE	VT-NUM3WALKS	VT-NUM4WALKS	VT-NUM5WALKS	VT-NUM6WALKS	VT-NUMNODES	VT-RANDICINDEX	VT-VORAREA	VT-VORPERIMETER									
vs. Subtypes	F1	F2	**	**	**	**	**	**	**	**	**	**	**	**	**	**	-	-	-	**	**	**	**	**	**	**	**	*	**	**	**	**	**	**	**	**	**	-	**								
	G2	**	**	**	**	**	**	**	**	**	**	**	**	**	**	**	**	**	**	**	**	**	**	**	**	**	**	**	*	**	**	**	**	**	**	**	**	**	**	**	**						
	H1	**	**	**	**	**	**	**	**	**	**	**	**	**	**	**	**	**	**	**	**	**	**	**	**	**	**	**	**	**	**	**	**	**	**	**	**	**	**	**	**	**					
	H2	**	**	**	**	**	**	**	**	**	**	**	**	**	**	**	**	**	**	**	**	**	**	**	**	**	**	**	**	**	**	**	**	**	**	**	**	**	**	**	**	**					
	I1	**	**	**	**	**	**	**	**	**	**	**	**	**	**	**	**	**	**	**	**	**	**	**	**	**	**	**	*	**	**	**	**	**	**	**	**	**	**	**	**	**					
	I2	**	**	**	**	**	**	**	**	**	**	**	**	**	**	**	**	**	**	-	**	**	**	**	**	**	**	**	**	**	**	**	**	**	**	**	**	**	**	**	**	**					
	F2	G1	**	**	**	**	**	**	**	**	**	**	**	**	**	**	**	**	**	**	**	**	**	**	**	**	**	**	**	**	**	**	**	**	**	**	**	**	**	**	**	**					
	G2	**	-	**	**	**	**	**	**	**	**	**	**	**	**	**	**	**	**	-	**	**	**	**	**	**	**	**	-	**	**	**	**	**	**	**	**	**	**	**	**	**					
	H1	**	**	**	**	**	**	**	**	**	**	**	**	**	**	**	**	**	**	**	**	-	**	**	**	**	**	**	**	**	**	**	**	**	**	**	**	**	**	**	**	**	**				
	H2	**	**	**	**	**	**	**	**	**	**	**	**	**	**	**	**	**	**	**	**	**	**	**	**	**	**	**	-	**	**	**	**	**	**	**	**	**	**	**	**	**	**				
	I1	**	-	**	**	**	**	**	**	**	**	**	**	**	**	**	**	**	**	-	**	**	**	**	**	**	**	**	-	**	**	**	**	**	**	**	**	**	**	**	**	**	**				
	I2	**	**	-	-	-	**	**	**	**	**	**	**	**	**	**	**	**	**	-	**	**	**	**	**	**	**	**	**	**	**	**	**	**	**	**	**	**	**	**	**	**	**	**			
	G1	G2	**	**	**	**	**	**	**	**	**	**	**	**	**	**	**	-	**	**	**	**	**	**	**	**	**	**	-	**	**	**	**	**	**	**	**	**	**	**	**	**	**	**			
	H1	**	**	**	**	**	**	**	**	**	**	**	**	**	**	**	**	**	**	**	**	**	**	**	**	**	**	**	**	**	**	**	**	**	**	**	**	**	**	**	**	**	**	**	**		
	H2	**	-	-	-	**	**	**	**	**	**	**	**	**	**	**	**	**	**	-	**	**	**	**	**	**	**	**	**	**	**	**	**	**	**	**	**	**	**	**	**	**	**	**	**		
	I1	**	**	*	**	**	**	**	**	**	**	**	**	**	**	**	**	**	**	**	**	**	**	**	**	**	**	**	**	**	**	**	**	**	**	**	**	**	**	**	**	**	**	**	**		
	I2	**	**	**	**	**	**	**	**	**	**	**	**	**	**	**	**	**	**	**	**	**	**	**	**	**	**	**	**	**	**	**	**	**	**	**	**	**	**	**	**	**	**	**	**	**	
	G2	H1	**	**	**	**	**	**	**	**	**	**	**	**	**	**	**	**	**	**	**	-	**	**	**	**	**	**	**	**	**	**	**	**	**	**	**	**	**	**	**	**	**	**	**		
	H2	**	**	**	**	**	**	**	**	**	**	**	**	**	**	**	*	**	**	**	**	**	**	**	**	**	**	**	-	*	**	**	**	**	**	**	**	**	**	**	**	**	**	**	**	**	
	I1	**	-	-	-	**	**	**	**	**	**	**	**	**	**	**	**	**	**	-	**	**	**	**	**	**	**	**	-	**	**	**	**	**	**	**	**	**	**	**	**	**	**	**	**	**	
I2	**	-	**	**	**	**	**	**	**	**	**	**	**	**	**	**	**	**	-	*	-	**	**	**	**	**	**	-	**	**	**	**	**	**	**	**	**	**	**	**	**	**	**	**	**		
H1	H2	**	**	**	**	**	**	**	**	**	**	**	**	**	**	-	**	**	**	**	**	**	**	**	**	**	**	-	**	**	**	**	**	**	**	**	**	**	**	**	**	-	**	**			
I1	**	**	**	**	**	**	**	**	**	**	**	**	**	**	**	**	**	**	**	**	-	**	**	**	**	**	**	**	**	**	**	**	**	**	**	**	**	**	**	**	**	**	**	**	**		
I2	**	**	**	**	**	**	**	**	**	**	**	**	**	**	**	**	**	**	**	**	-	**	**	**	**	**	**	**	**	**	**	**	**	**	**	**	**	**	**	**	**	**	**	**	**	**	
H2	I1	**	**	**	**	**	**	**	**	**	**	**	**	**	**	**	**	**	**	**	**	**	**	**	**	**	**	**	**	**	**	**	**	**	**	**	**	**	**	**	**	**	**	**	**	**	
I2	**	**	**	**	**	**	**	**	**	**	**	**	**	**	**	**	**	**	**	**	**	**	**	**	**	**	**	-	**	**	**	**	**	**	**	**	**	**	**	**	**	**	**	**	**	**	**
I1	I2	**	-	**	**	**	**	**	**	**	**	**	**	**	**	**	**	**	-	**	-	**	**	**	**	**	**	**	-	**	**	**	**	**	**	**	**	**	**	**	**	**	**	**	**	**	

Signif. codes: 0 '***' 0.01 '**' 0.05 '*' 1

Chapter 5

Concluding Remarks

5.1 Conclusion

The object of this thesis was to estimate which Glioma images have been grouped based on their pattern of the feature descriptors related to the region of nuclei. Glioma histopathological images for analyses were obtained from The Cancer Genome Atlas (TCGA) [13] database. Significant feature descriptors for Glioma images were determined and CellProfiler was employed to segment cell nuclei and extract features from the images. The heat-map was produced by Morpheus [33] to estimate which Glioma images have been grouped based on their pattern of the feature descriptors as subtypes.

As a result, Glioma could be categorized into 18 subtypes. In addition, the effectiveness of these features were investigated by Tukey–Kramer test. When taken together, all of the estimated subtypes were significantly different between each group. Furthermore, the result of this thesis indicates that most Spatial-Arrangement Features have meaningful information for subtypes clustering but most Object-Level Features not. Some Spatial-Arrangement Features were seen as being important to proceed advance researches, *e.g.* subtypes clustering.

5.2 Further Works

The final goal of our research is to specify subtypes of Glioma from histopathological images for precision medicine by genes expressions level. This thesis discussed about the subtypes of Glioma and showed that Glioma could be categorized into 18 subtypes by using cell nuclei features. The next work is to reduce dispersion in each TCGA data. In this study, 30 collected patches in each original images (total 6000 patches) were used as data-sets. Therefore, I will collect another 30 patches in each original images as data-set and do experiments. The future task is to confirm the relationships between the subtypes and the results of gene expression analysis.

Furthermore, as another our approach for this reseach, I proposed a disease stage classification method with Deep Learning for Glioma histopathological images [36]. In particular, Deep Convolutional Neural Network (Deep CNN) was employed as a Deep Learning model. By using the proposed method, I obtained a final average classification accuracy of 96.5%. The next step of this approach is to discover not cell nuclei features but other feature descriptors. this thesis just focused on feature descriptors related to the region of nuclei, and it is hard to know whether these features are perfect for histopathological image analysis or not. Other feature descriptors might be required for more advanced analysis. By using Deep Learning method, feature descriptors are extracted from the data (*e.g.* image, sound) without human intervention. Therefore, other feature descriptors might be discovered by analyzing our Deep CNN configuration. I hope these approaches will be of help in medical decision analysis of brain tumors.

Acknowledgement

First of all, I really would like to express my deepest gratitude to Prof. Shinji Tsuruoka, who is the Executive Vice-President of Mie University and Associate Prof. Hiroharu Kawanaka at Graduate School of Engineering, Mie University who offered continuing supports and constant encouragements.

I am also grateful to Prof. Bruce J. Aronow and Prof. V. B. Surya Prasath at Cincinnati Children's Hospital Medical Center, USA. They provided a lot of technical help and encouragement. Prof. Aronow accepted me as a short-term study abroad student at his laboratory in Cincinnati Children's Hospital Medical Center. Thanks to his help and encouragement, I was able to make good progress in my project. Prof. Surya gave me a lot of technical and language help in my research project and writing papers.

In addition, this study was partially supported by Mie University study abroad program. Thanks to this program, I could stay Cincinnati Children's Hospital Medical Center for a month to obtain great progress and discuss the project with experts. I would like to sincerely thank this scholarship program. And finally, I would like to appreciate other members related my research project.

Reference

- [1] A. M. Marchevsky and M. R. Wick, “Evidence-based medicine, medical decision analysis, and pathology”, *Human Pathology*, vol. 35, no. 10, pp. 1179–1188, 2004.
- [2] L. E. Boucheron, “Object-and spatial-level quantitative analysis of multispectral histopathology images for detection and characterization of cancer”, Ph. D. dissertation, University of California, Santa Barbara, CA, 2008.
- [3] Bilgin C., Demir C., Nagi C. and Yener B., “Cell-graph mining for breast tissue modeling and classification”, 29th Annual International Conference of the IEEE Engineering in Medicine and Biology Society (EMBS), Proc. IEEE, pp. 5311-5314, 2007.
- [4] K. Rodenacker and E. Bengtsson, “A feature set for cytometry on digitized microscopic images”, *Analytical Cellular Pathology* 25, pp. 1-36, 2003.
- [5] O. Sertel, J. Kong, U. V. Catalyurek, G. Lozanski, J. H. Saltz, M. N. Gurcan, “Histopathological Image Analysis Using Model-Based Intermediate Representations and Color Texture: Follicular Lymphoma Grading”, *Journal of Signal Processing Systems*, vol.55, no. 169, 2009.
- [6] K. T. Zondervan, N. Rahmioglu, A. P. Morris, D. R. Nyholt, G. W. Montgomery, C. N. Becker, S. A. Missmer, “Beyond Endometriosis Genome-Wide Association Study: From Genomics to Phenomics to the Patient”, *Seminars in Reproductive Medicine*, vol. 34, no. 4, pp. 242-254, 2016.
- [7] J. Xu, T. Shao, N. Ding, Y. Li, X. Li, “miRNA-miRNA crosstalk: from genomics to phenomics”, *Briefings in Bioinformatics*, vol. 18, no. 6, pp. 1002-1011, 2017.
- [8] R. A. Hegele and R. L. Pollex, “Hypertriglyceridemia: phenomics and genomics”, *Mol Cell Biochem*, vol.326 , no. 1-2, pp. 35-43, 2009.
- [9] L. Chin, J. A. Wargo, D. J. Spring, H. Kantarjian, P. A. Futreal, “Cancer Genomics in Clinical Context”, *Trends in Cancer*, vol.1, no. 1, pp. 36-43, 2015.
- [10] K. Fukuma, H. Kawanaka, V. B. S. Prasath, B. J. Aronow, H. Takase, “Feature extraction and disease stage classification for glioma histopathology images”, *IEEE International Conference on E-health Networking, Application & Services (Health-Com)*, Proc. IEEE, pp. 429–430, 2015.

- [11] K. Fukuma, H. Kawanaka, V. B. S. Prasath, B. J. Aronow, H. Takase, “A study on feature extraction and disease stage classification for glioma pathology images”, IEEE International Conference on Fuzzy Systems (FUZZ-IEEE), Proc. IEEE, 2016.
- [12] K. Fukuma, V. B. S. Prasath, H. Kawanaka, B. J. Aronow, H. Takase, “A study on nuclei segmentation, feature extraction and disease stage classification for human brain histopathological images”, 20th International Conference on KnowledgeBased and Intelligent Information & Engineering Systems (KES-2016), Proc. IEEE, pp. 1202-1210, 2016.
- [13] NIH THE CANCER GENOME ATLAS. “<https://cancergenome.nih.gov/>” (accessed 2018/12/10)
- [14] K. Tomczak, P. Czerwińska, M. Wiznerowicz, “The Cancer Genome Atlas (TCGA): an immeasurable source of knowledge”, Journal of Contemporary Oncology, vol. 19, no. 1A, A68–A77, 2015.
- [15] M. R. Lamprecht, D. M. Sabatini, A. E. Carpenter, “CellProfiler: free, versatile software for automated biological image analysis”, BioTechniques, vol. 42, no. 1, pp. 71–75, 2007.
- [16] A. E. Carpenter, T. R. Jones, M. R. Lamprecht, C. Clarke, I. H. Kang, O. Friman, D. A. Guertin, J. H. Chang, R. A. Lindquist, J. Moffat, P. Golland and D. M. Sabatini, “CellProfiler: image analysis software for identifying and quantifying cell phenotypes”, Genome Biology, vol. 7, no. 10, R100, 2006.
- [17] V. B. S. Prasath and R. Delhibabu, “Image restoration with fuzzy coefficient driven anisotropic diffusion”, Joint International Conference on Swarm, Evolutionary and Memetic Computing (SEMCCO), Proc. Springer LNCS 8947, pp. 145–155, 2014.
- [18] V. B. S. Prasath and R. Delhibabu, “Automatic mucosa detection in video capsule endoscopy with adaptive thresholding”, International Conference on Computational Intelligence in Data Mining (ICCIDM), Proc. Springer SIST 410, pp. 95–102, 2015.
- [19] Kiichi Fukuma, Hiroharu Kawanaka, V. B. Surya Prasath, Bruce J. Aronow and Haruhiko Takase, “A Study on Accuracy of Nuclei Segmentation for Tissue Specimen Analysis of Brain Histopathology Images”, The Seventh International Workshop on Regional Innovation Studies (IWRIS2015), #6, pp.21-24, 2015.
- [20] M. N. Gurcan, L. E. Boucheron, A. Can, A. Madabhushi, N. M. Rajpoot, and B. Yener, “Histopathological image analysis: A review”, IEEE Reviews In Biomedical Engineering, vol. 2, pp. 47–171, 2009.

- [21] A. Yonekura, H. Kawanaka, V. B. S. Prasath, B. J. Aronow, and S. Tsuruoka, "Glioma Subtypes Clustering Method using Histopathological Image Analysis", in the 7th International Conference on Informatics, Electronics & Vision (ICIEV), Proc. IEEE, pp. 442-446, 2018.
- [22] A. Yonekura, H. Kawanaka, V. B. S. Prasath, B. J. Aronow, and S. Tsuruoka, "A Proposal on the Glioma Subtypes Clustered Method Using Histopathology Image Analysis", Fuzzy System Symposium 2018 (FSS), p. 875, 2018.
- [23] B. Weyn, W. A. A. Tjalma, P. Vermeulen, A. van Daele, E. va. Marck, and W. Jacob, "Determination of tumour prognosis based on angiogenesis-related vascular patterns measured by fractal and syntactic structure analysis", *Clinical Oncology*, vol. 16, pp.307-316, 2004.
- [24] B. Weyn, G. van de Wouwer, S. Kumar-Singh, A. van Daele, P. Scheunders, E. van Marck, and W. Jacob, "Computer-assisted differential diagnosis of malignant mesothelioma based on syntactic structure analysis", *Cytometry*, vol. 35, pp. 23-29. 1999.
- [25] J. F. O'Callaghan, "Computing the perceptual boundaries of dot patterns", *Computer Graphics and Image Processing*, vol. 3, pp. 141-162, 1974.
- [26] R. Marcelpoil and Y. Usson, "Methods for the study of cellular sociology: Voronoi diagrams and parametrization of the spatial relationships", *Journal of Theoretical Biology*, vol. 154, pp. 359-369, 1992.
- [27] M. Hummel, D. Edelmann, A. Kopp-Schneider, "Clustering of samples and variables with mixed-type data", *PLoS One*, vol. 12, no. 11, e0188274, 2017.
- [28] N. Novoselova, J. Wang, F. Klawonn, "Optimized leaf ordering with class labels for hierarchical clustering", *J Bioinform Comput Biol*, vo. 13, no. 4, 1550012, 2015.
- [29] J. Gu, M. Pitz, S. Breitner, W. Birmili, S. V. Klot, A. Schneider, J. Soentgen, A. Reller, A. Peters, J. Cyrus, "Selection of key ambient particulate variables for epidemiological studies - applying cluster and heatmap analyses as tools for data reduction", *Science of The Total Environment*, vol. 435-436, pp. 541-550, 2012.
- [30] J. W. Lee, K. M. Cho, J. H. Jung, Q. Tran, W. Jung, J. Park, K. P. Kim, "Alteration of Phospholipids during the Mitophagic Process in Lung Cancer Cells", *J Microbiol Biotechnol*, vol. 26, no. 10, pp. 1790-1799, 2016.
- [31] X. Wang, A. H. Liu, Z. W. Jia, K. Pu, K. Y. Chen, H. Guo, "Genome-wide DNA methylation patterns in coronary heart disease", *Herz*, vol. 43, no. 7, pp. 656-662, 2018.

- [32] A. Bergkvist, V. Rusnakova, R. Sindelka, J. M. Garda, B. Sjögreen, D. Lindh, A. Forootan, M. Kubista, “Gene expression profiling—Clusters of possibilities”, *Mol Cell Biochem*, vol. 326, no. 1-2, pp. 35-43, 2009.
- [33] Morpheus. “<https://software.broadinstitute.org/morpheus>” (accessed 2018/12/10)
- [34] J. W. Tukey, “Comparing Individual Means in the Analysis of Variance”, *International Biometric Society*, Vol. 5, No. 2, pp. 99-114, 1949.
- [35] C. Y. Kramer, “Extension of Multiple Range Tests to Group Means with Unequal Numbers of Replications”, *International Biometric Society*, Vol. 12, No. 3, pp. 307-310, 1956.
- [36] A. Yonekura, H. Kawanaka, V. B. S. Prasath, B. J. Aronow, H. Takase, “Automatic disease stage classification of glioblastoma multiforme histopathological images using deep convolutional neural network”, *Biomedical Engineering Letters*, Volume 8, Issue, 3, pp. 321–327, 2018.

Publication List

Journal Paper

(1) A. Yonekura, H. Kawanaka, V. B. S. Prasath, B. J. Aronow, H. Takase, "Automatic disease stage classification of glioblastoma multiforme histopathological images using deep convolutional neural network," *Biomedical Engineering Letters*, Volume 8, Issue 3, pp 321–327, 2018.

International Conferences

(1) A. Yonekura, H. Kawanaka, V. B. S. Prasath, B. J. Aronow, and H. Takase, "Disease stage classification for Glioblastoma Multiforme histopathological images using deep convolutional neural network," in *Joint 17th World Congress of International Fuzzy Systems Association and 9th International Conference on Soft Computing and Intelligent Systems (IFSA-SCIS)*, #270, 2017.

(2) A. Yonekura, H. Kawanaka, V. B. S. Prasath, B. J. Aronow, and H. Takase, "Glioblastoma Multiforme Tissue Histopathology Images Based Disease Stage Classification with Deep CNN," in the *6th International Conference on Informatics, Electronics & Vision (ICIEV)*, #111, 2017.

(3) A. Yonekura, H. Kawanaka, V. B. S. Prasath, B. J. Aronow, and H. Takase, "A Study on Convolutional Neural Network for Disease Stage Classification of Glioma Tissue Images," *The 7th International Symposium for Sustainability by Engineering at Mie University (Research Area C) (IS2EMU2017-C)*, A-20, 2017.

(4) A. Yonekura, H. Kawanaka, V. B. S. Prasath, B. J. Aronow, and H. Takase, "A Proposal for Automatic Disease Stage Classification in Glioma Histopathology Images Using Deep CNN," *The 9th International Workshop on Regional Innovation Studies (IWRIS)*, pp. 20-23, 2017.

(5) A. Yonekura, H. Kawanaka, V. B. S. Prasath, B. J. Aronow, and H. Takase, "Improving the Generalization of Disease Stage Classification with Deep CNN for Glioma

Histopathological Images,” International Workshop on Deep Learning in Bioinformatics, Biomedicine, and Healthcare Informatics (DLB2H) in conjunction with the IEEE International Conference on Bioinformatics and Biomedicine (BIBM), pp. 1203-1207, 2017.

(6) A. Yonekura, H. Kawanaka, V. B. S. Prasath, B. J. Aronow, and H. Takase, ”Automatic Disease Stage Classification of Brain Glioblastoma Multiforme Histopathological Images using Deep Convolutional Neural Networks,” Machine Learning in Science and Engineering (MLSE), 2018.

(7) A. Yonekura, H. Kawanaka, V. B. S. Prasath, B. J. Aronow, and S. Tsuruoka, ”Glioma Subtypes Clustering Method using Histopathological Image Analysis,” in the 7th International Conference on Informatics, Electronics & Vision (ICIEV), #237, 2018.

(8) A. Yonekura, H. Kawanaka, V. B. S. Prasath, B. J. Aronow, and S. Tsuruoka, ”Subtypes Clustered Method for Glioblastoma Multiforme Tissue Images Using Cell Nuclei Features,” The 8th International Symposium for Sustainability by Engineering at Mie University (Research Area C) (IS2EMU2018-C), A-1, 2018.

Domestic Conferences

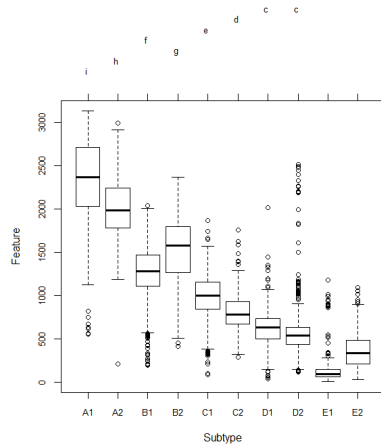
(1) 米倉朝美, 川中普晴, V. B. Surya Prasath, Bruce J. Aronow, 高瀬治彦, “Deep Learning を用いた脳組織病理画像の疾患進行度評価に関する研究 (A Study on Disease Stage Classification for Human Brain Histopathological Images using Deep Learning)”, 平成29年度電気・電子・情報関係学会東海支部連合大会講演論文集, F5-2, 2017.

(2) 米倉朝美, 川中普晴, V. B. Surya Prasath, Bruce J. Aronow, 高瀬治彦, 鶴岡信治, “畳み込みニューラルネットワークを用いた神経膠腫の病理画像に対する疾患進行度評価法に関する一検討 (A Proposal for Disease Stage Evaluation in Glioma Images using Convolutional Neural Network)”, 平成29年度日本生体工学会東海支部学術集会予稿集, p. 21, 2017.

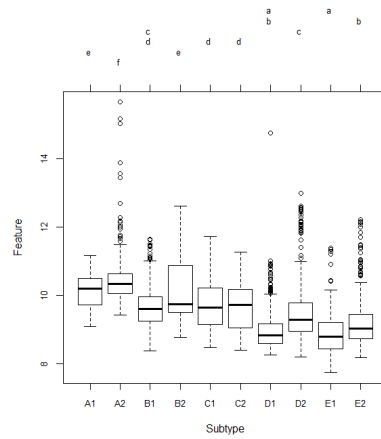
(3) 米倉朝美, 川中普晴, V. B. Surya Prasath, Bruce J. Aronow, 鶴岡信治, “組織病理画像解析結果を用いた神経膠腫のサブタイプ分類に関する一検討 (A Proposal on the Glioma Subtypes Clustered Method Using Histopathology Image Analysis)”, 第34回ファジィシステムシンポジウム FSS2018, p. 875, 2018.

Appendix A

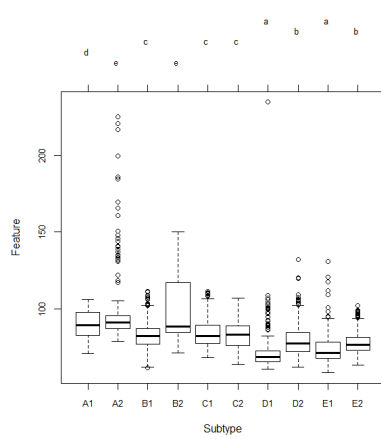
Results of Boxplot (GBM)



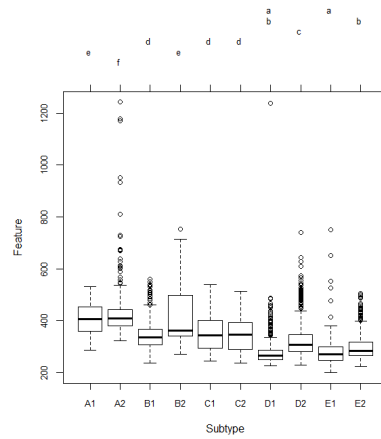
(1) Area



(2) BF-PERIMETERCURVATURE

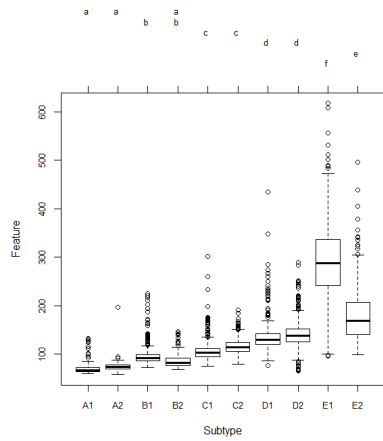


(3) BF-RADII

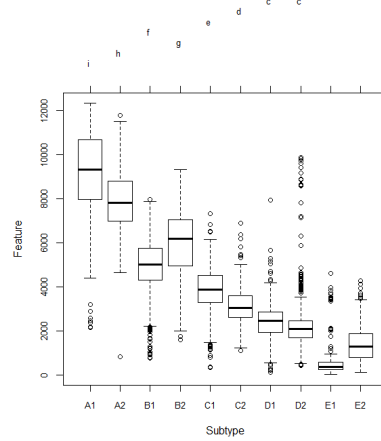


(4) CH-CONVEXDEFICIENCY

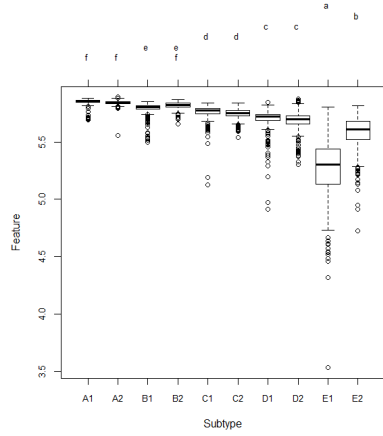
Figure A.1: Boxplots of GBM (1)-(4).



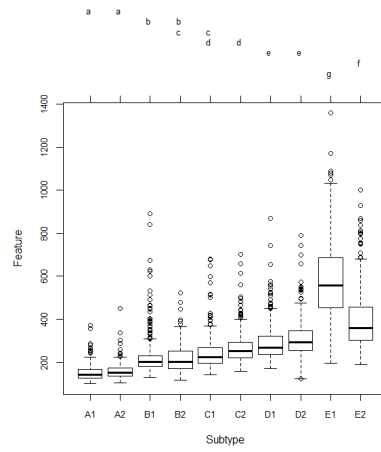
(5) DT-AVEEDGELENGTH



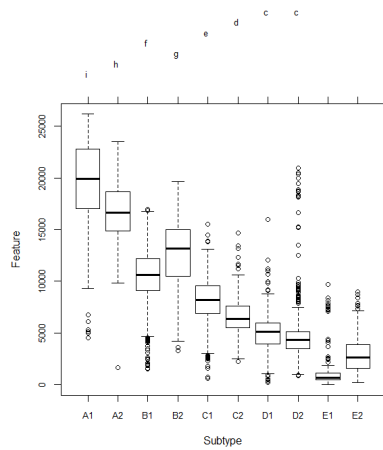
(6) DT-CYCLONUM



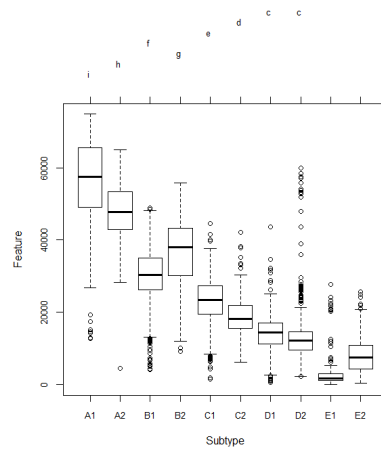
(7) DT-DEGREE



(8) DT-MAXEDGELENGTH

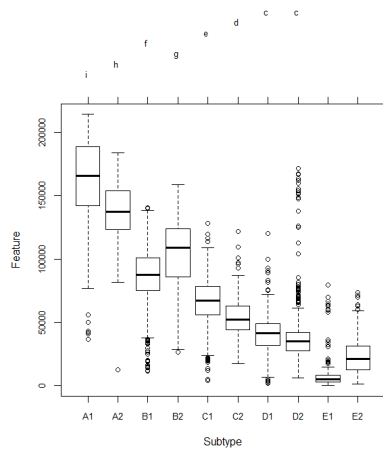


(9) DT-NUM3WALKS

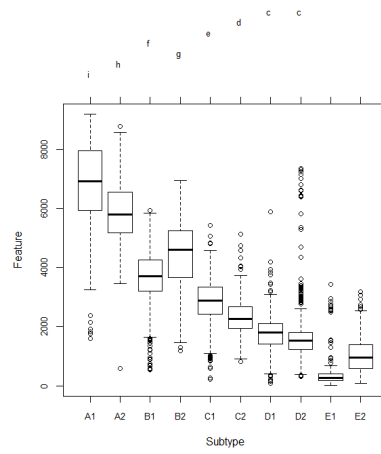


(10) DT-NUM4WALKS

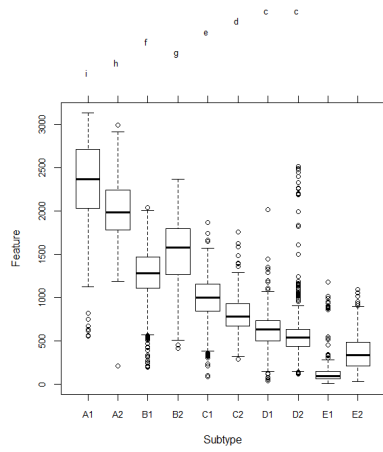
Figure A.2: Boxplots of GBM (5)-(10).



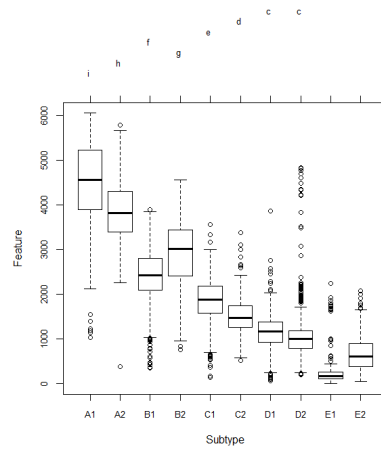
(11) DT-NUM5WALKS



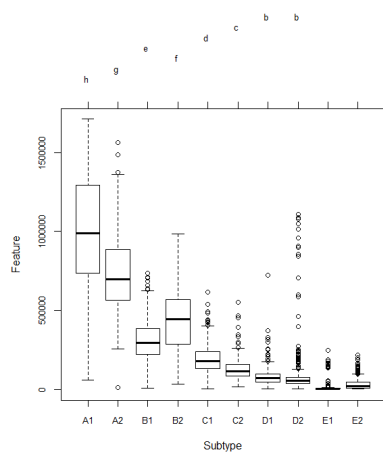
(12) DT-NUMEDGES



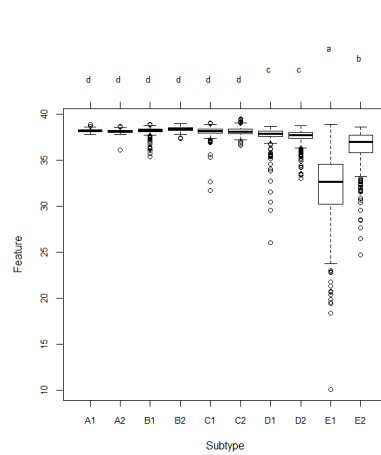
(13) DT-NUMNODES



(14) DT-NUMTRIANGLES

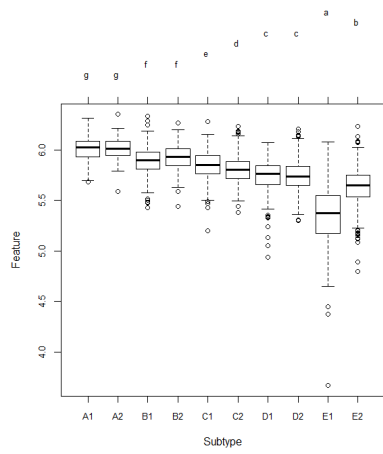


(15) DT-RANDICINDEX

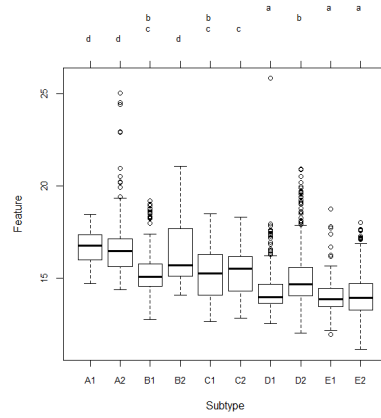


(16) DT-SPECTRALRADIUS1

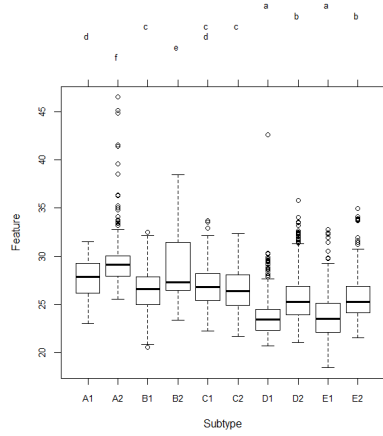
Figure A.3: Boxplots of GBM (11)-(16).



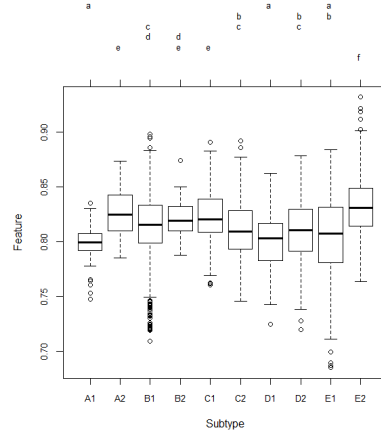
(17) DT-SPECTRALRADIUS2



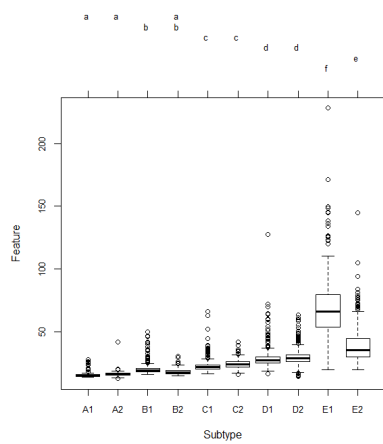
(18) EL-ECCENTRICITY



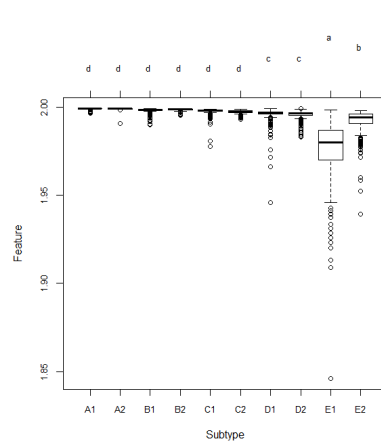
(19) EL-MINORLENGTH



(20) EL-ORIENTATION

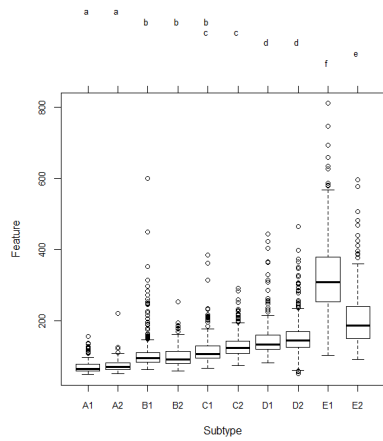


(21) MST-AVEEDGELENGTH

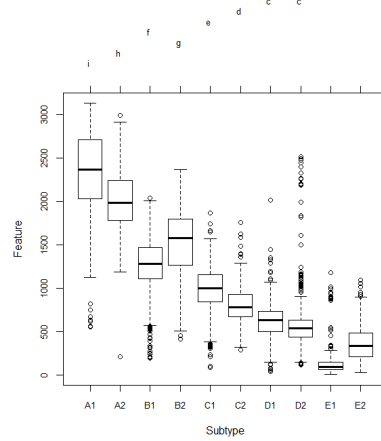


(22) MST-DEGREE

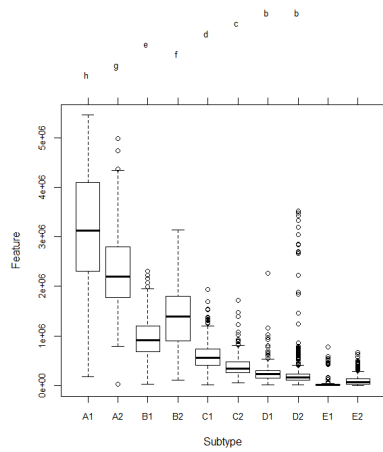
Figure A.4: Boxplots of GBM (17)-(22).



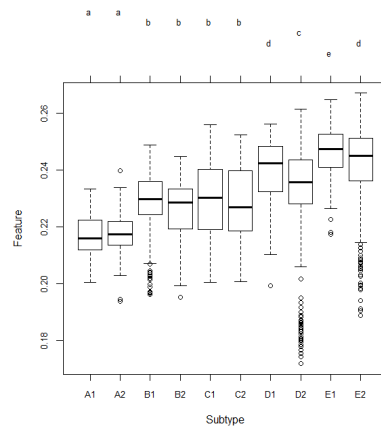
(23) MST-MAXEDGELENGTH



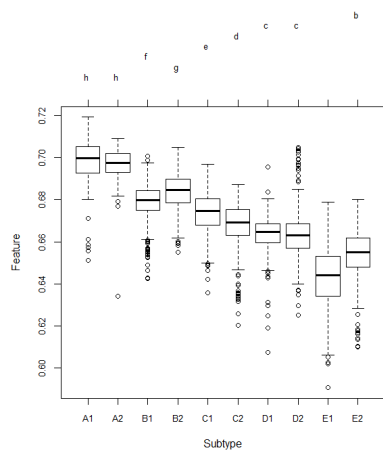
(24) MST-NUMNODES



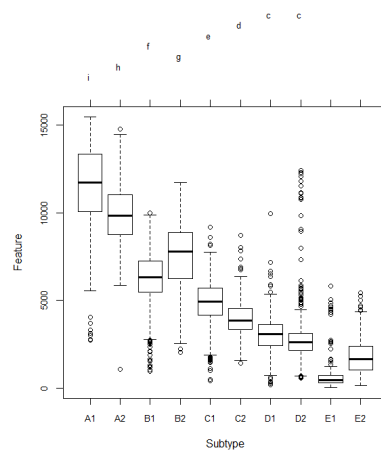
(25) MST-RANDICINDEX



(26) OS-SPHERICITY

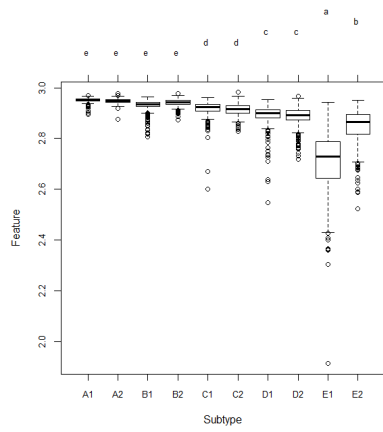


(27) VT-AVEROUNDFACTOR

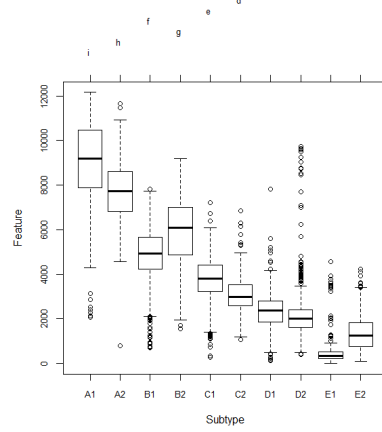


(28) VT-CYCLONUM

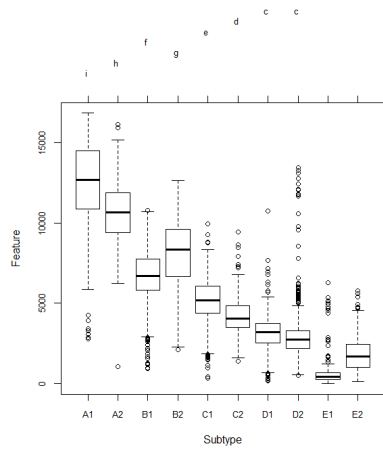
Figure A.5: Boxplots of GBM (23)-(28).



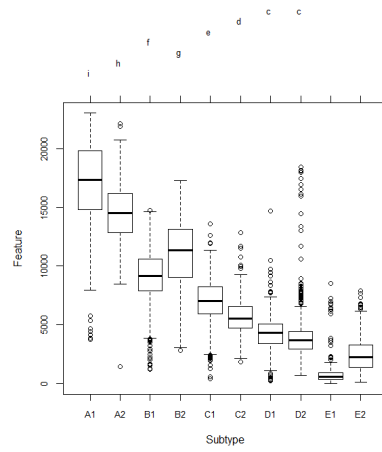
(29) VT-DEGREE



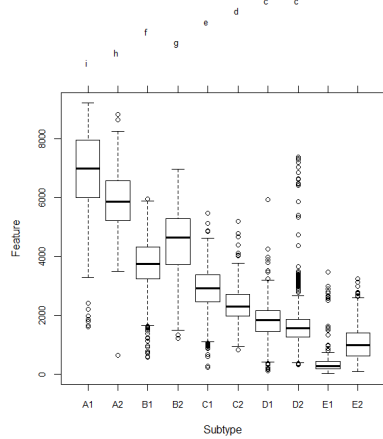
(30) VT-NUM3WALKS



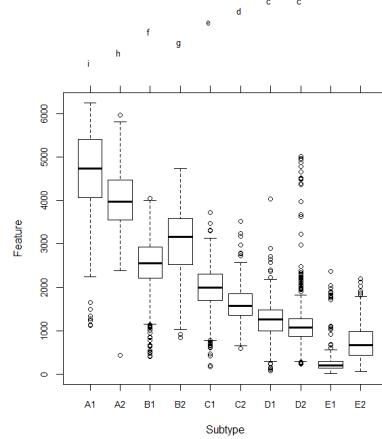
(31) VT-NUM4WALKS



(32) VT-NUM5WALKS

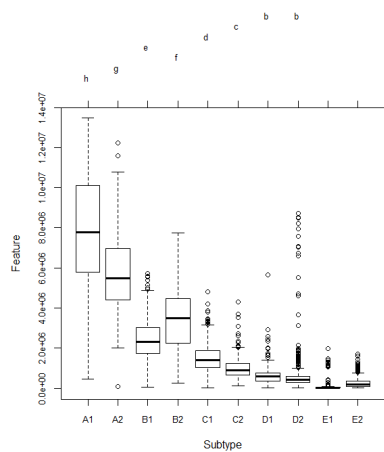


(33) VT-NUMEDGES

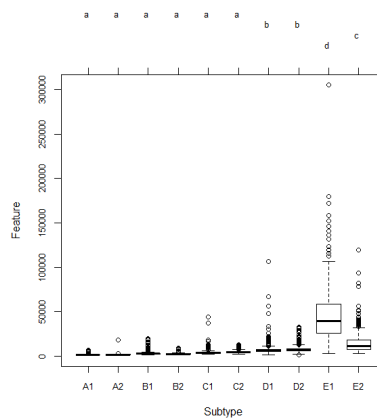


(34) VT-NUMNODES

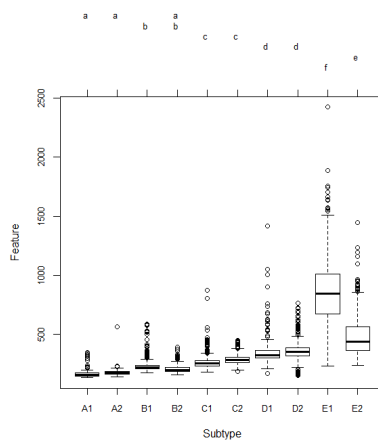
Figure A.6: Boxplots of GBM (29)-(34).



(35) VT-RANDICINDEX



(36) VT-VOROAREA

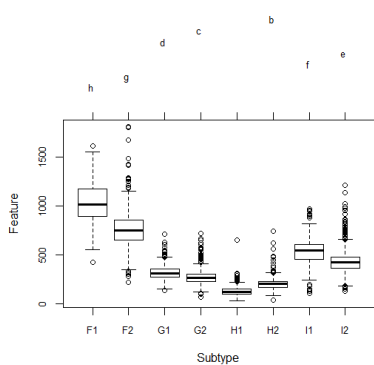


(37) VT-VOROPERIMETER

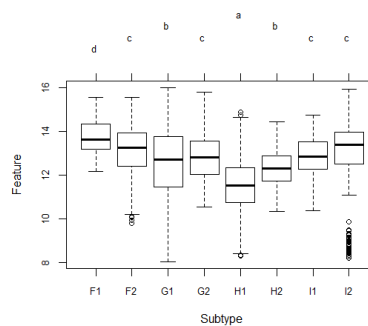
Figure A.7: Boxplots of GBM (35)-(37).

Appendix B

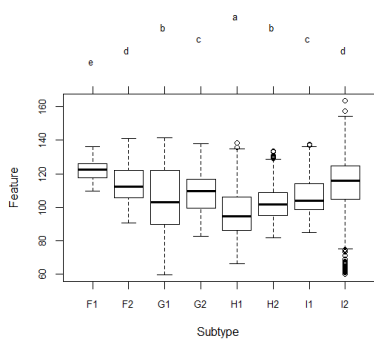
Results of Boxplot (LGG)



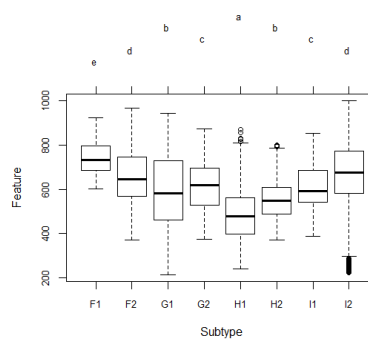
(1) Area



(2) BF-PERIMETERCURVATURE

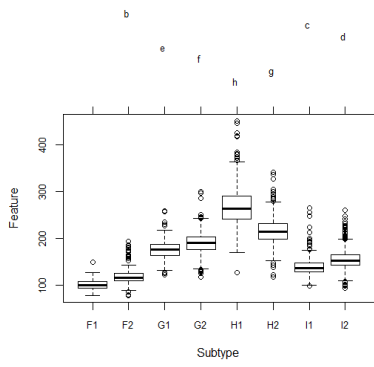


(3) BF-RADII

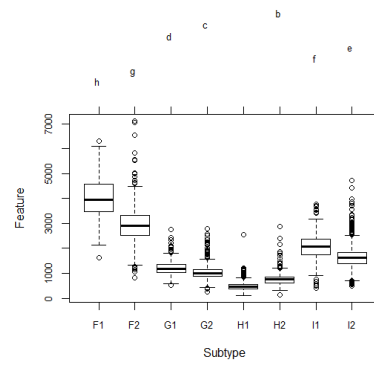


(4) CH-CONVEXDEFICIENCY

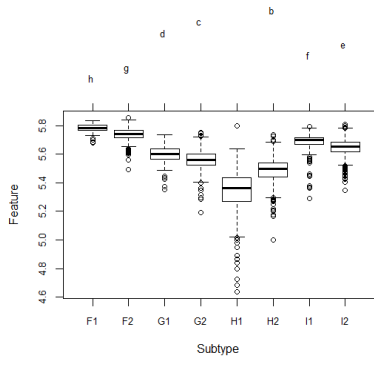
Figure B.1: Boxplots of LGG (1)-(4).



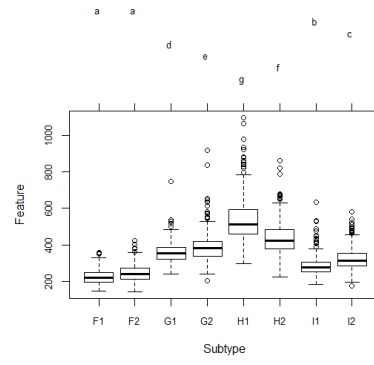
(5) DT-AVEEDGELENGTH



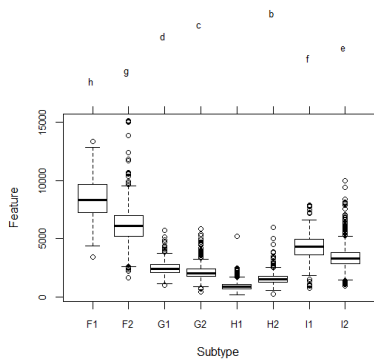
(6) DT-CYCLONUM



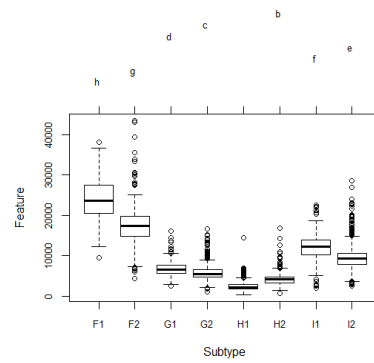
(7) DT-DEGREE



(8) DT-MAXEDGELENGTH

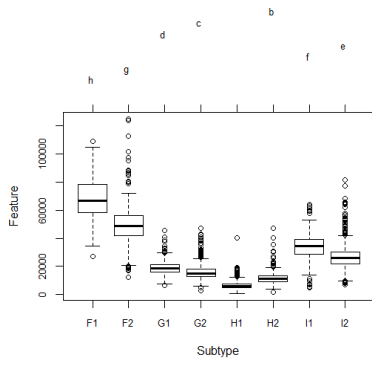


(9) DT-NUM3WALKS

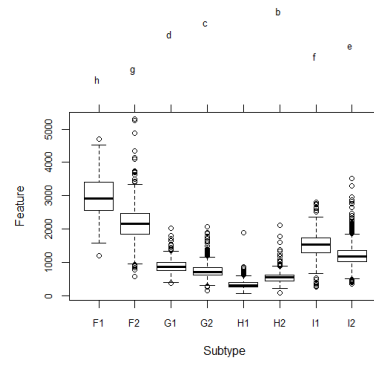


(10) DT-NUM4WALKS

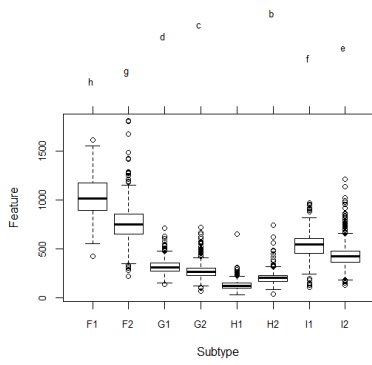
Figure B.2: Boxplots of LGG (4)-(10).



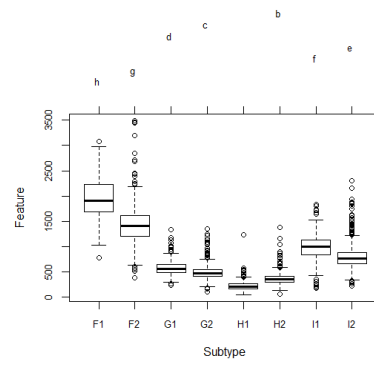
(11) DT-NUM5WALKS



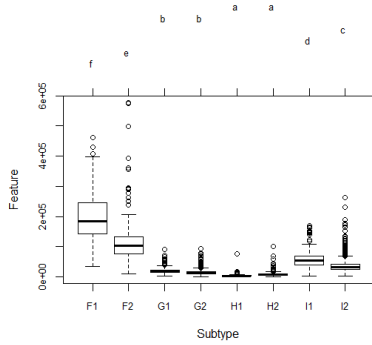
(12) DT-NUMEDGES



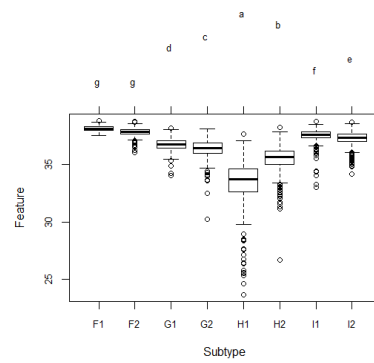
(13) DT-NUMNODES



(14) DT-NUMTRIANGLES

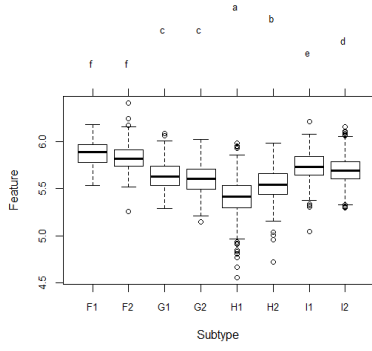


(15) DT-RANDICINDEX

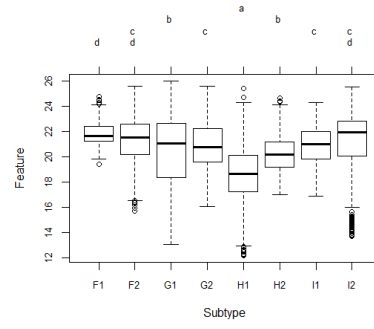


(16) DT-SPECTRALRADIUS1

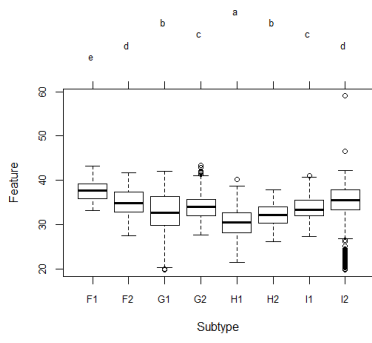
Figure B.3: Boxplots of LGG (11)-(16).



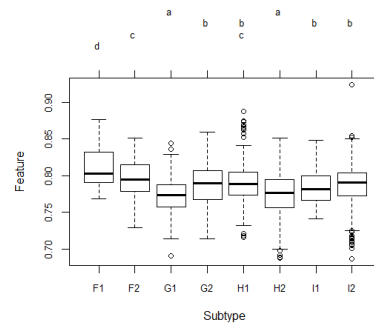
(17) DT-SPECTRALRADIUS2



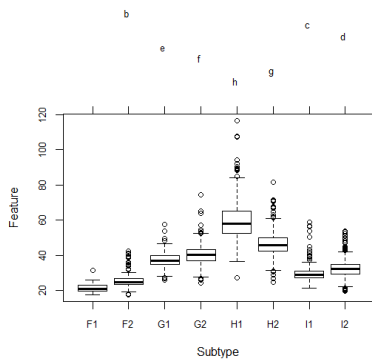
(18) EL-ECCENTRICITY



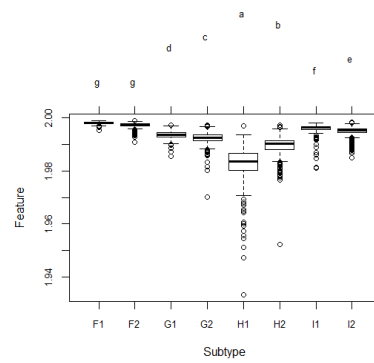
(19) EL-MINORLENGTH



(20) EL-ORIENTATION

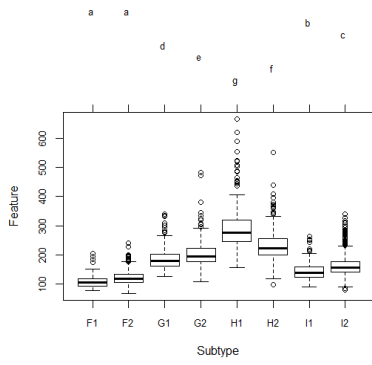


(21) MST-AVEEDGELENGTH

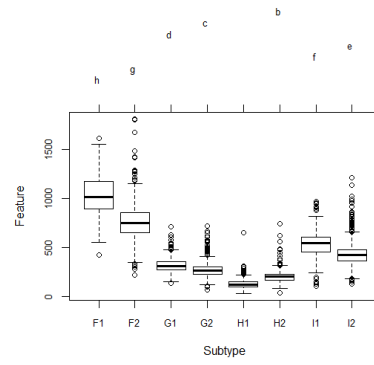


(22) MST-DEGREE

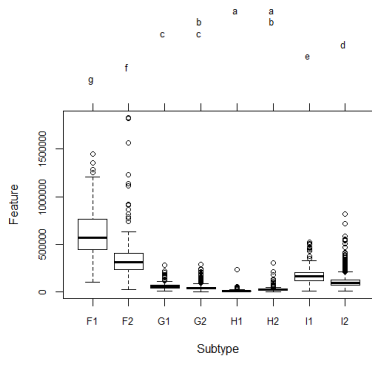
Figure B.4: Boxplots of LGG (17)-(22).



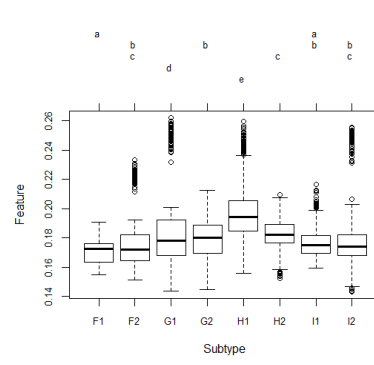
(23) MST-MAXEDGELENGTH



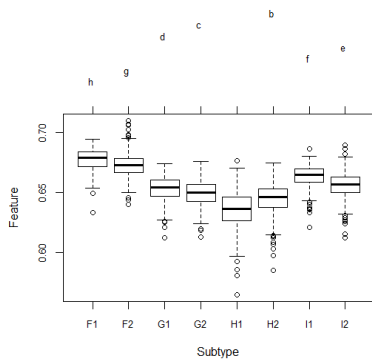
(24) MST-NUMNODES



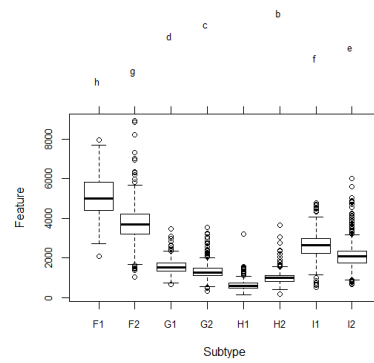
(25) MST-RANDICINDEX



(26) OS-SPHERICITY

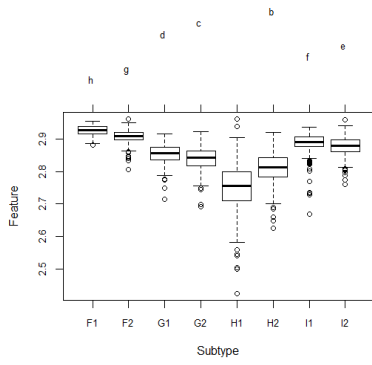


(27) VT-AVEROUNDFACTOR

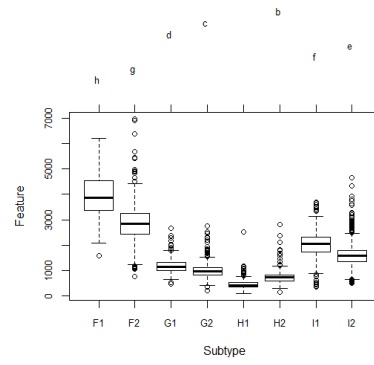


(28) VT-CYCLONUM

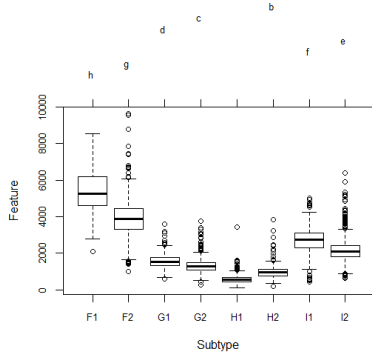
Figure B.5: Boxplots of LGG (23)-(28).



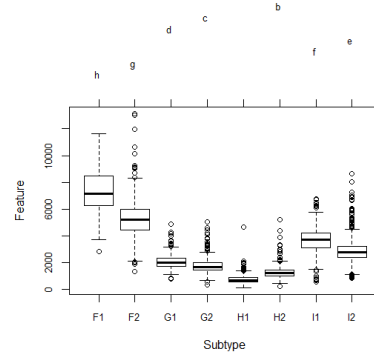
(29) VT-DEGREE



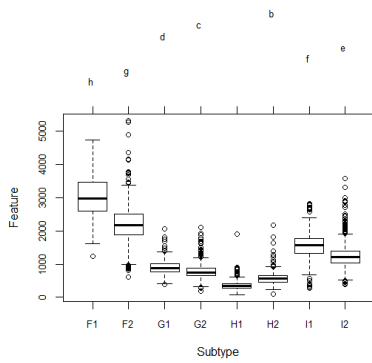
(30) VT-NUM3WALKS



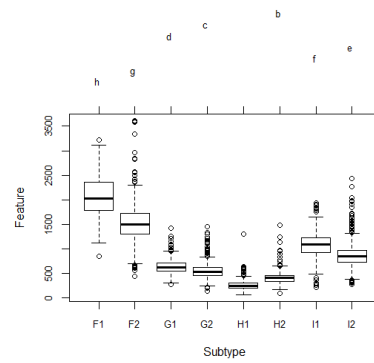
(31) VT-NUM4WALKS



(32) VT-NUM5WALKS

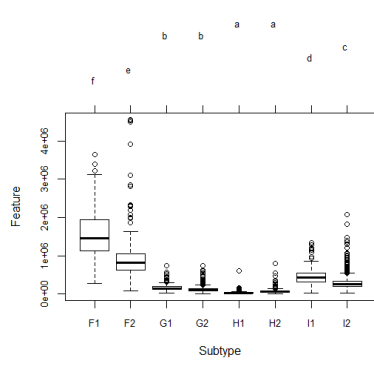


(33) VT-NUMEDGES

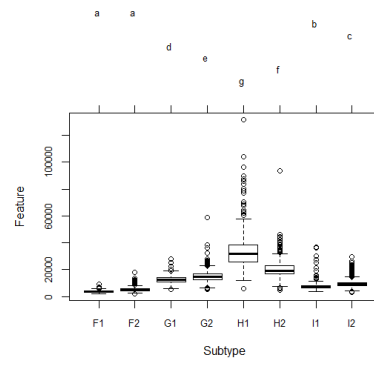


(34) VT-NUMNODES

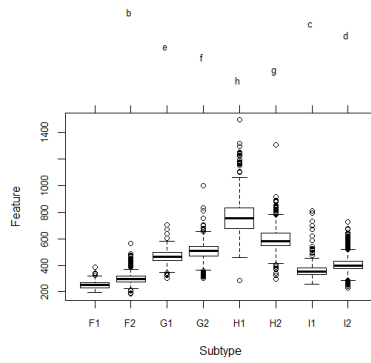
Figure B.6: Boxplots of LGG (29)-(34).



(35) VT-RANDICINDEX



(36) VT-VOROAREA



(37) VT-VOROPERIMETER

Figure B.7: Boxplots of LGG (35)-(37).